VASCULAR EXPANSION MICROSCOPY (VASCEXM): A NEW METHOD FOR HIGH-RESOLUTION OPTICAL IMAGING OF THE MICROVASCULATURE.

by
Nausheen Tickoo

A thesis submitted to Johns Hopkins University in conformity with the requirements for the degree of Master of Science and Engineering

Baltimore, Maryland
July 2020

Abstract

Purpose: The resolution of optical images systems is restricted by the diffraction limit. In the past two decades super resolution microscopy techniques have been developed to circumvent this limitation. However, these techniques depend on state-of-the-art technological advancements. In 2015, the Boyden Lab at MIT developed a technique called expansion microscopy (ExM) which allows nanoscale resolution imaging of tissue samples using conventional diffraction-limited microscopes by physically expanding the specimen. Samples are embedded within polyelectrolyte gels that get deprotonated in a basic environment; this cause the gel to swell in solutions like water. The hydrogel expands, expanding the sample along with it, increasing the distance between closely placed structures, thereby resolving them. This thesis aims to develop a tissue processing protocol, based on ExM, for high-resolution 3D optical imaging of the vasculature in preclinical models and to optimize this protocol across various vascular labels.

Methods: 10-100 μn sections of the brain, liver, lung, heart, and leg muscle of C57 BALB/c mice were individually labeled with Tomato Lectin Tx-Red, Anti-Laminin Cy3 and a BriteVu and Galbumin-Rhodamine polymer complex to compare the vasculature pre-and post-expansion. Morphological parameters such as mean vessel diameter, area and volume were obtained by vascular segmentation using IMARIS ® to quantify the expansion process.

Results: Similar trends were observed post-expansion in the mean vessel diameter across the different organs. A magnification of ~2.5x was observed in the mouse brain, leg, and liver vasculature while a ~1.6x magnification was observed in lung vasculature. However, due to sampling error expansion was not observed in the vasculature of mouse heart tissue samples.

Conclusion: Developed a new expansion protocol, VascExM, to obtain high resolution 3D images of the Tomato Lectin Tx-Red labelled mouse vasculature using diffraction limited microscopes.

Primary Reader and Advisor: Arvind Pathak
Secondary Readers: Kristine Glunde and Shuli Xia

Acknowledgements

This thesis would not have been possible without the guidance and support of my advisor, colleagues, friends, and family.

I would like to express by deepest gratitude to my thesis advisor, **Dr. Arvind Pathak**, who gave me the opportunity to work on this project. His expert guidance consistently helped steer the project in the right direction. His feedback and mentorship enabled me to develop a deeper understanding of the subject.

I am grateful to all of those in **the Pathak Lab** with whom I have had the pleasure of working, especially **Dr. Akanksha Bhargava**, for her insightful suggestions and discussions, specifically regarding image preprocessing and segmentation. I sincerely appreciate her guidance particularly during my initial days in the lab. I also appreciate **Dr. Janaka Senarathna's** help in animal procurement and handling.

Furthermore, I would also like to thank **Dr. Kristine Glunde** and **Dr. Shuli Xia** for agreeing to be on my committee and offering their valuable inputs on the project.

Lastly, I must express my very profound gratitude to my **friends and family**. To Ankita, Akansha, Monika, Akanksha and Sanjana for always lending an ear especially during these uncertain and isolating times. And most importantly, to the six pillars in my life, badi mama, ma, papa, choti mama, chotey papa and Tamanna, for providing me with unfailing support and continuous encouragement throughout my life and especially through the process of writing this thesis. This accomplishment would not have been possible without them.

This thesis is dedicated to my grandfather, J.L. Tickoo.

Table of Contents

List of Tables

List of Figures

INTENDED TO BE BLANK

CHAPTER 1: INTRODUCTION

1.2 Expansion Microscopy: A new method for circumventing the diffraction limit in optical imaging

The resolving power of an optical imaging system is limited by the diffraction of the light. The diffraction limit (or Abbe limit) is the smallest distance between two objects that can be resolved by the system. It is determined by λ/2NA, where λ is the wavelength of the light and NA is the numerical aperture of the lens. Due to this phenomenon, a microscope is not able to resolve two objects if they are located at a distance that is shorter than λ/2NA [1]. Scientists have developed numerous methods to circumvent this limit. In recent years, several super-resolution fluorescence microscopy techniques have been invented to overcome this limit. For example, some non-linear methods include, stimulated emission depletion (STED) microscopy achieves this by using a laser to suppress the emission from fluorophores not located at the center of the point of excitation [2]. Reversible saturable optical fluorescence transitions (RESOLFT) uses fluorescent probes which switch between fluorescent state and dark state thus requiring low laser intensity which leads to a low residual fluorescence level [3]. Saturated pattern excitation microscopy (SPEM) and saturated structured illumination microscopy (SSIM) deplete the fluorophore ground state by saturated excitation to generate a sinusoidal emission pattern that is recorded by a detector. And some stochastic techniques like photo-activated localization microscopy (PALM or fPALM) and stochastic optical reconstruction microscopy (STORM), widefield fluorescence microscopy that relies on the stochastic activation of fluorescence to intermittently photoswitch individual photoactivatable molecules to a bright state, which are then imaged and photobleached, allowing temporary separation of very closely spaced molecules [4].

Recently, expansion microscopy (ExM), a new technique developed by the Edward Boyden Lab at MIT in 2015 improves the magnification of optical microscopy, not from the instrumentation aspect but from the perspective of the specimen being imaged. The Boyden team's method involved improving the spatial resolution of microscopy by expanding the sample specimen rather than investing in more powerful microscopes. ExM merges two scientific concepts, the first is the property of polyelectrolyte hydrogels to expand when immersed in solvents such as water, and the second is the process of embedding the sample in polymer hydrogels for imaging [5]. Thus, ExM enhances the spatial resolution and makes finer structural details of the sample visible by using an expandable polymer network which physically expands the specimen embedded within it by ~4.5×. Fluorescent-dye conjugated antibodies bound to molecules of interest are covalently attached to the polymer network, thus when the polymer swells, the specimen anchored to it undergoes isotropic expansion and optical labels close to the optical diffraction limit are resolved. ExM enables the use of conventional microscopes for better resolved images [6]. Recently, nanoscale-resolution ExM has been optimized for imaging proteins, RNA in preserved cells and tissue in a protocol dubbed as proExM and ExFISH, respectively [5][6].

ProExM or Protein retention Expansion Microscopy (**Fig.1**) resolves images of proteins that have been covalently bound to a hydrogel matrix using Acryloyl-X Succinimidyl Ester (SE). The SE interacts with the amines in proteins, to copolymerize into the polyacrylamide matrix. This embedded sample undergoes enzymatic digestion when submerged in a solution containing Proteinase K (ProK). This protease homogenizes the mechanical characteristics of the tissue – polymer composite causing isotropic expansion of the composite when it is immersed in water. According to Chen et al, fluorescent antibodies survive the proteolysis process, therefore

permitting ProExM to be conducted on samples which have been labeled before or after expansion [6][7].

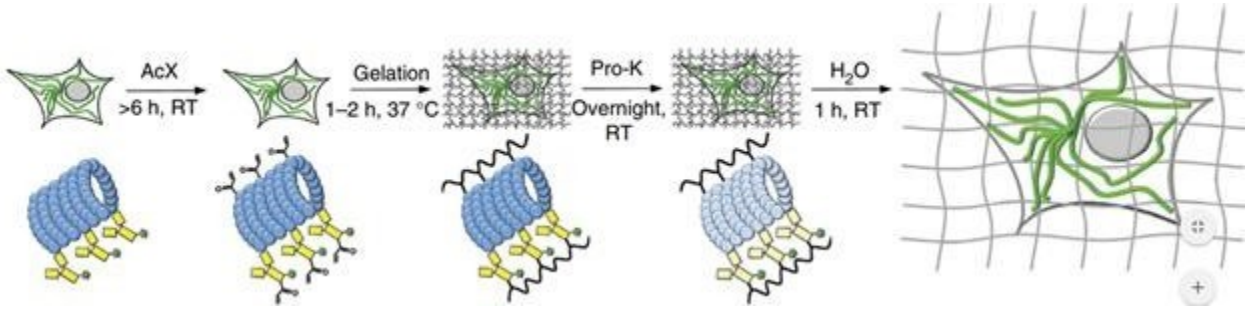

Fig 1. Protein retention ExM (proExM) workflow adapted from Asano et al [7]. Samples are fixed and stained with antibodies using conventional immunostaining protocols, then treated at room temperature with Acryloyl-X SE, which enables proteins to be anchored to the hydrogel. The samples then undergo gelation, proteinase K (ProK) treatment for digestion, and finally expansion in water.

In contrast, expansion fluorescence in situ hybridization (ExFISH) is used to image RNA molecules. Like ProExM, ExFISH involves anchoring of RNA to the polymer matrix by covalently binding to Label X (a combination of LabelIT amine and AcX/DMSO solution) – used in place of Acryloyl-X Succinimidyl Ester. The Label X binds to the RNA at Guanine from one end and to the polymer at the other. Once the matrix is formed, proteolyzed using ProK and washed with PBS, fluorescent probes are used to bind with RNA molecules in the sample and then expanded. The composite is imaged while placed in a low-salt buffer to maintain stability of the anchored RNA probes.[7]

These original protocols have been further developed over the years. Chang et al, detail the development of what is described as iterative expansion microscopy (iExM) [8]. Initial research was conducted to explore the possibility to expand a standard ExM gel to greater than ~4.5× magnification. However, the hydrogel once expanded to greater than 4.5× became very fragile and did not provide the required mechanical support. A second method was implemented wherein the

hydrogel was synthesized using a cleavable crosslinker. Using a cleavable crosslinker ensured that the sample stayed expanded while a second conventional crosslinker was formed around it. At a high pH, the diol bonds in the first gel get cleaved and the gel dissolves, leaving only the second conventional crosslinker to be expanded in water. The second gel expands the specimen another ~4×, for a total increase of ~16-22×. Chang et al implemented iExM to visualize synaptic proteins and the architecture of dendritic spines in the mouse brain [8].

To date ExM has been optimized to visualize microtubules [6], synaptic proteins [7], RNA [7], lipids [9], lesions in cancerous and normal clinical samples from organs such as the prostate, breast and lung tissue [10]. Imaging these organs and visualizing important architectures using ExM has led to nanoscale resolution images while reducing the cost of using high power microscopes. However, as of August 2019 ExM had not been employed to visualize the vasculature. **Therefore, this thesis describes the development of a new tissue processing protocol for high-resolution optical imaging of the vasculature in preclinical tissue samples. We have dubbed this protocol: vascular expansion microscopy (VascExM).**

1.3 Current Techniques for Imaging the Vasculature:

1.3.1 Computed Tomography (CT)

Developed in the early 70's by Godfrey Hounsfield and James Ambrose, CT uses ionizing radiation (i.e. x-rays) which are beamed through the specimen at multiple projections. These issue-attenuated x-ray beams are then detected by an electronic detector array. The greater the density

of the object or tissue, the greater the x-ray attenuation. The internal structure of the tissue is then reconstructed using these multiple projection views of the recorded x-ray density patterns [11].

Over the years, as the technology behind CT has advanced significantly many variations have been developed, notably reducing the radiation dose and the time it takes to acquire hundreds of high-resolution thin-slice images to a few short seconds, compared to the tens of minutes for considerably low-resolution ones taken with the earlier iterations. Most commonly, the vasculature has been imaged by CT angiography [12], micro-CT [16,17,18,19,20,21], nano-CT [22,23]. In vivo CT scanning is used for longitudinal studies whereas ex vivo CT scanning is preferred for endpoint studies.

Clinical CT is a significant technological development that can show weak, damaged inflamed and blocked blood vessels [13]. Clinical CT can show structural and functional aspects of the vascular system, therefore helping doctors to diagnose vascular diseases and disorders. CT angiography is used to characterize the vascular structure around the heart [14]. Other research has been conducted for peripheral vascular disease to identify blockage in blood vessels including deep vein thrombosis and to find aneurysms and bulges that might lead to burst blood vessels [15].

Due to their smaller scale preclinical models like mouse and rat require advanced CT scanning that can resolve vasculature at a micro- or nanoscale (**Fig 2**). Contrast-enhanced micro-CT enables 3D imaging with high spatial resolution (1-100 μm) and permits the differentiation of vessels in both in vivo and ex vivo studies of preclinical models. Currently, an *in vivo* micro-CT scanner has resolutions ranging from 100 to 30 μm, while *ex vivo* scanners have resolutions from 30 to 1 μm [16]. Micro-CT has been successful in quantifying pulmonary volume in the microvasculature of a mouse lung to evaluate pro-angiogenic therapies in pre-clinical models of

vascular disease [17], visualizing and quantifying whole tumor vasculature for the study of tumor angiogenesis [18,19] and blood flow [20] and 3D cerebral vasculature atlases which are a significant resource for future studies [21].

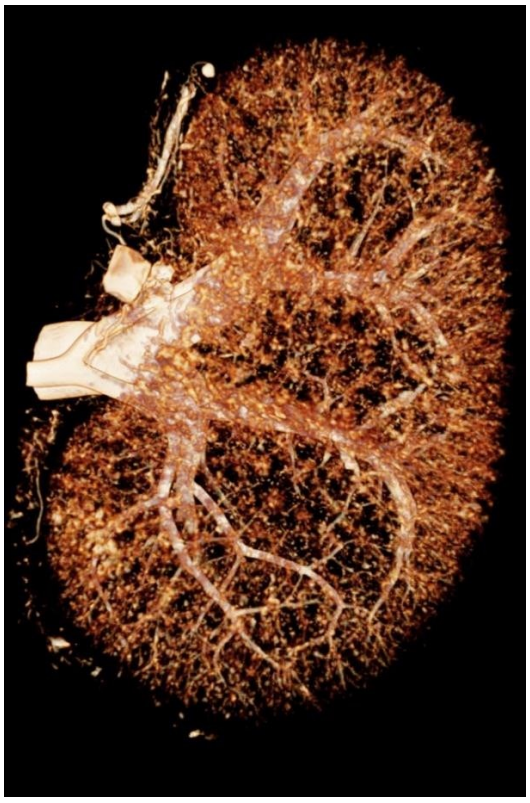

Fig 2. Visualizing microvasculature in a mouse kidney using micro-CT imaging. Positive vascular contrast is achieved on micro-CT imaging by perfusing the vasculature with a polymer mixture that contains 1:4.5 radiopaque BriteVu® in water and a Galbumin – Rhodamine (0.96mg/ml) based contrast agent. In the μmCT image, glomeruli are revealed at a resolution of 7.5 μm. Figure adapted from Bhargava et al, The FASB Journal (2020).

The main drawback of micro-CT imaging is poor soft tissue contrast. This technique requires the use of a contrast agent without which blood vessels cannot be differentiated from other soft tissue. Thus, the imaging modality can be limited by the properties of the contrast agent used. For example, insufficient contrast agent may result in low SNR images that are not easy to analyze or quantify. However, a more critical limitation of micro-CT is the lack of advanced analysis and quantification software for the analysis of the dense architecture of blood vessels, limiting its use to primarily image bones [22].

Nano-CT is the promising new high-resolution cross-sectional imaging technique that was developed by enhancing the established micro-CT technology. Currently, nano-CT has the capability to image objects with the spatial resolution of up to 400nm [23]. Comparison of the vasculature in the cerebral cortex of a transgenic mouse model indicates the improved detectability of the details of the smaller structures, and increased sharpness of the edges visualized objects regardless of the size. This gives a more precise structural information about the vessel [24].

1.3.2 Magnetic Resonance Imaging (MRI)

MRI, is a non-invasive imaging technology, produces 2D and 3D anatomical images by employing powerful magnets to create strong magnetic fields. The static magnetic field forces water protons in the tissue to align with it. A radiofrequency wave is then pulsed through the patient to excite the magnetization of the water protons momentarily. The recovery or "relaxation" of this "induced" tissue magnetization can then be detected with an antenna and converted to an image by the simultaneous imposition of magnetic gradients during the acquisition. Analogous to CT, one can employ MRI contrast agents, generally Gadolinium (Gd)-based to image the vasculature. Unlike CT, MRI uses "non-ionizing" radiation that makes it safer for use [25].

Some of the latest research in imaging and studying the vasculature is being done using MRI. While there is a large variety of MRI techniques, ex vivo imaging of vasculature in preclinical models is primarily conducted by the following techniques: Magnetic resonance angiography (MRA), susceptibility weighted imaging (SWI), and intercranial vessel wall imaging (IVW).

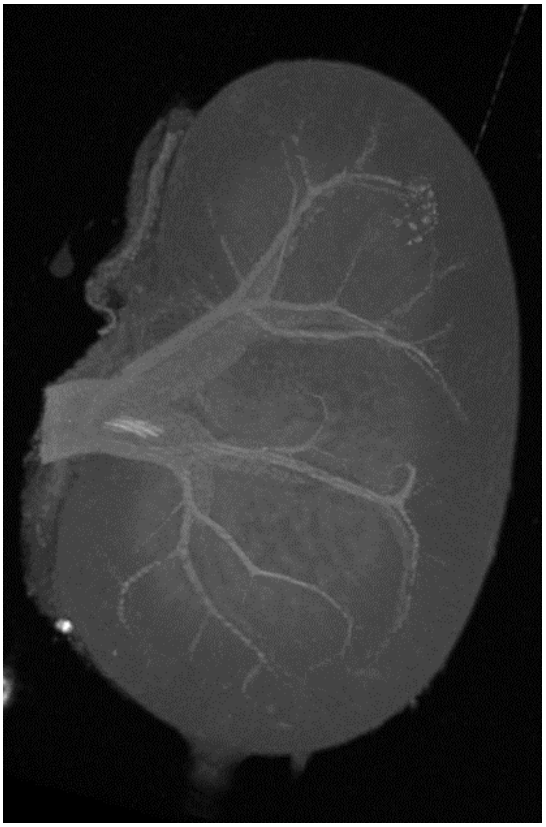

Fig 3. Visualizing microvasculature in a mouse kidney using MRI imaging. Positive vascular contrast is achieved on MRI imaging by perfusing the vasculature with a polymer mixture that contains 1:4.5 radiopaque BriteVu® in water and a Galbumin – Rhodamine (0.96mg/ml) based contrast agent. Here large vessels in the kidney can be visualized with MRI at 60μm. Figure adapted from Bhargava et al, The FASB Journal (2020).

1.3.2.1 Magnetic Resonance Angiography (MRA):

MRA can be categorized into two types based on their working principle: 1) flow based, which includes time-of-flight (TOF) MRA and phase contrast (PC) MRA. In flow-based techniques, scanners use motion of blood flowing in the vessels for detection.

Time-of-flight (TOF) MRA results when MR contrast differentiates the flowing blood from stationary tissue by manipulating its magnetization. The stationary tissue being imaged, is magnetically saturated by applying multiple RF pulses, while the fresh inflowing blood that gets imaged experiences fewer RF pulses causing it to have a higher initial magnetization level.

Therefore, the highly magnetized inflowing blood appears brighter than the saturated background tissue. TOF MRA can be categorized into 2D - obtained by imaging multiple 1-3mm thick slices with short pulses, usually less than 30ms. 2D TOF is preferred for its short imaging time, sensitivity to areas of slow blood flow and ability to expand area of imaging by adding more slices of the sample; and 3D - offering high spatial resolution and SNR while imaging small multiplanar areas, with limited speed of acquisition [26]. A study conducted by Brubaker et al shows that high resolution 3D TOF MRA images at 3T can be used to visualize and classify tumor and normal vasculature in transgenic mice [27]. Ultra-high field (7T) TOF MRA captures the cerebral microvasculature, enabling the visualization of even minute brain lesions [28].

Phase contrast (PC) MRA distinguishes between flowing blood from stationary tissue by manipulating the phase of the magnetization. PC is based on the phase shift acquired by spins moving along a magnetic field gradient [29]. PC MRA can be used to quantify blood flow and wall shear stress. However, because of relatively high blood velocities relative to the size of the mouse anatomy, signal loss from spin dephasing can be a significant problem in mouse MRA, particularly in regions of vessel curvature therefore it is not a common choice [30]

Contrast enhanced (CE) MRA: As the name suggests, CE MRA employs a contrast agent (usually a Gadolinium-chelate), injected into the circulatory system to generate high vessel-to-background contrast. The presence of Gadolinium within vessels ensures that the vascular signal on CE MRA is not hampered by the numerous flow-related artifacts such as signal loss from spin saturation or slow flow that can degrade flow-based MRA techniques [31]. Multiple comparative studies [32] have been conducted that determine the Contrast-enhanced MRA offers better diagnostic accuracy than TOF-MRA, superior localizing capability of vessel occlusion within a

shorter acquisition time while providing a larger coverage. In addition, Bullitt *et al*. shows that CE MRA can be used to detect and quantify changes in the 3-D morphology of blood vessels [33].

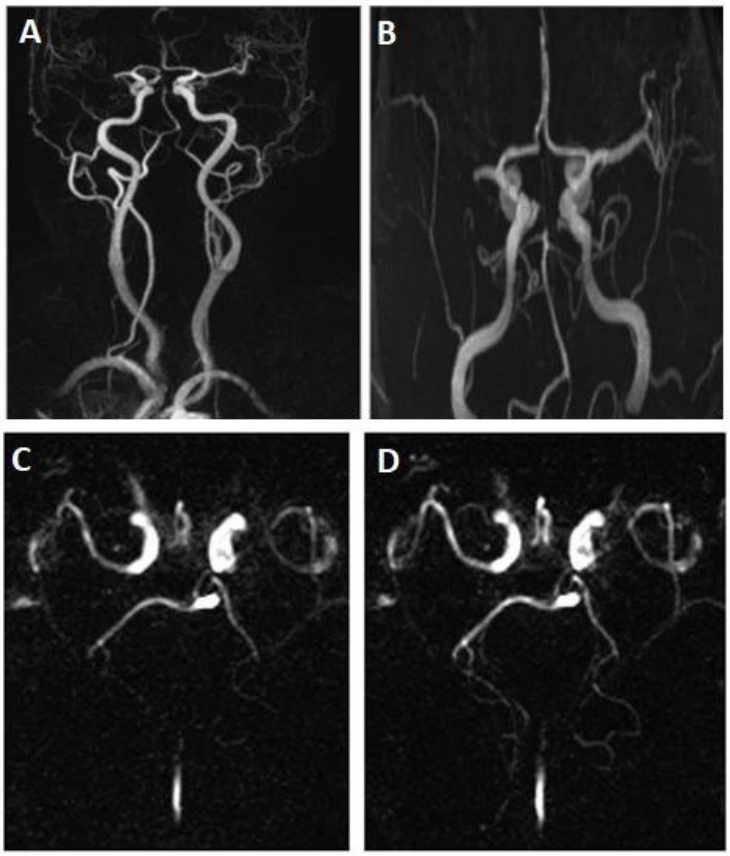

Fig 4. TOF-, PC- and CE-MRA. (A and B) CE-MRA and TOF-MRA shows an occlusion of right M1 segment of a 72 -year old woman with acute stroke symptoms before treatment, respectively [Adapted from T. Boujan et al, 2018. 33]. (C and D) PC- MRA and Gadolinium administered CE- MRA, due to shortening of T1 an improvement is seen in the SNR enabling detection of smaller vessels [30]. Compared to TOF-MRA and PC-MRA, CE-MRA shows a significant improvement in distinguishing smaller structures.

1.3.2.2 Susceptibility – Weighted Imaging (SWI)

SWI is an MRI sequence that exploits the difference in magnetic susceptibility of various compounds to provide phase maps with improved contrast-to-noise ratio of the desired biomolecule in an MRI. Thus, it is ideal for detecting compounds such as blood, iron, and calcium

[34]. SWI has been helpful in detecting micro-and macro-hemorrhages, identifying cerebral microvasculature and malformations in low blood flow vessels [34]. An increase in vessel visibility was noted when SWI was used to indicate the presence of ischemia in a post-blast acute phase of injury in rat models [35]. It was similarly used to assess the vascular and tissue changes post transient cerebral ischemia in a study conducted on mouse models [36].

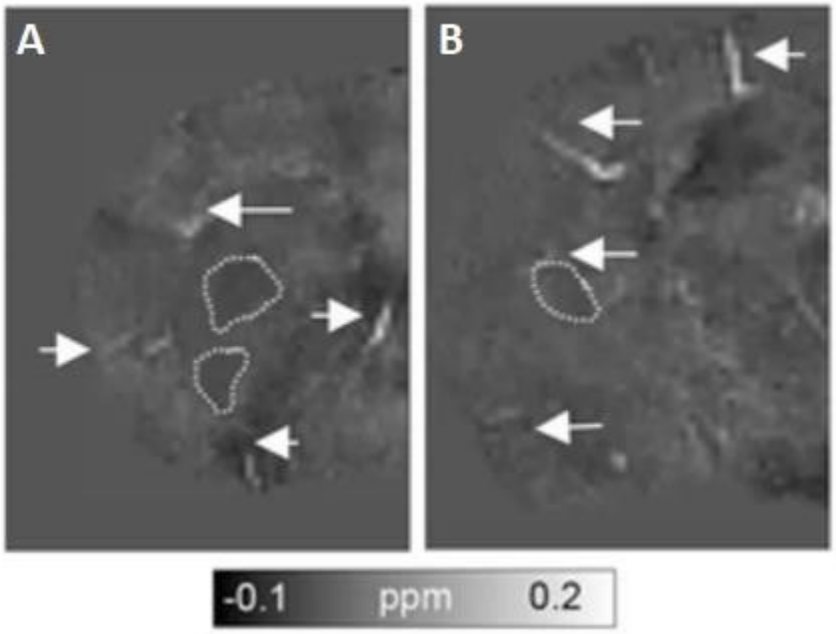

Fig 5. Cross-sections quantitative susceptibility maps (QSM) of the ischemic hemisphere of a tMCAO mouse after 48 h of reperfusion. White arrows mark the vessels while lesions are marked by the dotted white lines which were observed to be visible more prominently at longer time intervals of reperfusion. Figure adapted from M. Vaas et al, 2018 [36].

1.3.3 Small Animal Positron Emission Tomography (PET) and Single Photon Emission Tomography (SPECT)

PET utilizes tracers or contrast agents that contain specially designed radioactive molecules, such as Fluorine-18. Cyclotrons are used to generate the radioactive atoms, which are

then attached to the specific biomolecule required to be identified in the PET scan. The patient is injected with this radioactive molecule or radiotracer. Once inside the patient's circulatory system, the biomolecule creates a positron when the radioactive atom decays. This positron collides with an electron in the circulatory system, thereby annihilating each other to release two (511 keV) photons of γ-rays ($\lambda <= 1nm$) in opposite directions. The PET scanner detects these two photons to determine the exact location of their origin. Thousands of these emissions can be detected in a short period of time, allowing the sensors to recreate a 3D image of the location of the radiotracer distribution in the animal [37]. Small-animal PET has high sensitivity and the ability to provide quantitative, *in vivo* measurement of changes to the cerebral blood flow, glucose metabolism, and protein synthesis in the mouse brain microenvironment [38]. PET has also been used commonly along with CT and to generate multi modal nuclear images for cardiovascular diseases [39] and image the angiogenesis process at a molecular level in the mouse model [39]. PET/CT was also used to successfully study the varying degrees of human lung tumor vascularization established in a rat model. The PET scans also contributed to characterization of the tumors [40].

SPECT also uses radioactive tracers to create 3D images like PET. However, SPECT scans utilize a single gamma ray ($\lambda <= 1nm$) which are emitted from the injected radiotracers, such as iodine-123 and iodine -131 [41]. Along with a longer half-life SPECT also differs from PET in its spatial resolution, the systems have 12-15 mm and 1-2 mm spatial resolution, respectively. Latest preclinical applications of SPET include monitoring angiogenesis to evaluate efficacy of therapeutic interventions for cardiovascular diseases [42], 3-D visualization of the architecture of intramyocardial vessels during systole and diastole in rats [43].

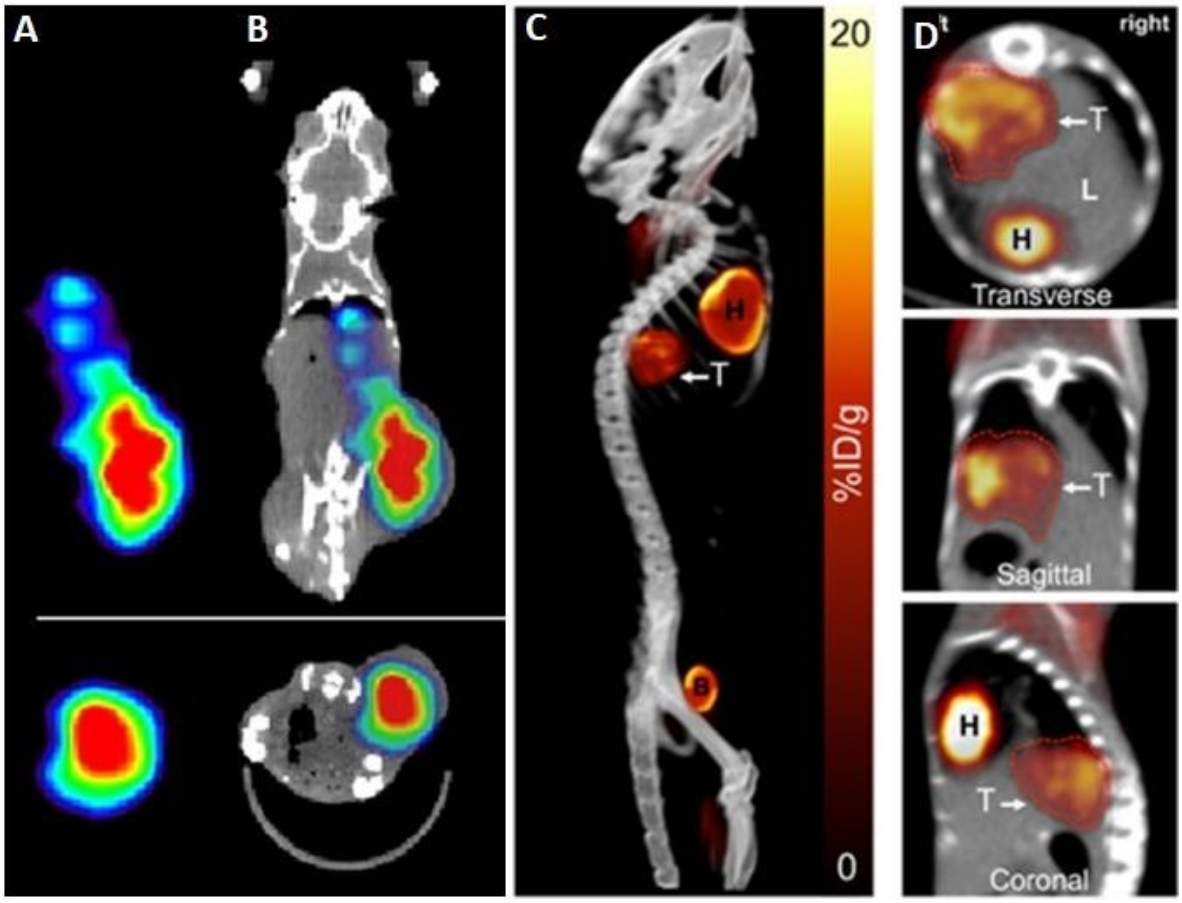

Fig 6. Small-animal SPECT/CT and PET/CT. (A and B) Coronal (top) and trans axial (bottom) images from study of LNCaP prostate cancer xenograft model 72 h after administration of antibody to PSMA labeled with ^{177}Lu. (A) SPECT image of tumor uptake. (B) Tumor uptake localized on SPECT/CT overlay images [44]. (C and D) ^{18}F-FDG PET image of glucose transporter 1 (Glut1) expression in FDG avid Lkb1 *Lkb1*$^{-/-}$ (KL) mutant lung tumors. (C) MIP of 3D reconstruction (D) MIP of transverse, sagittal and coronal views of lung tumor (T) [45].

CHAPTER 2: Methods and Protocols for VascExM

2.1 Table of Reagents Used

Reagent	Manufacturer	Concentration
Phosphate-buffered Saline (PBS)	Quality Biological, Inc. Gaithersburg, MD	1×
Buffered Formalin	Sigma Aldrich, Saint Louis, MO	10%
Sucrose	Sigma Aldrich, Saint Louis, MO	30%
Liquid Nitrogen	Sigma Aldrich, Saint Louis, MO	As required
Optimal cutting temperature compound (OCT)	Sakura Finetek, Torrance, CA	As required
Triton X-100	Thermo Fisher Scientific, Rockford, IL	0.1%
Carbo-free blocking solution	Vector Laboratories, Burlingame, CA	1mg/ml
Acryloyl-X SE (AcX)	Thermo Fisher Scientific, Rockford, IL	1mg/ml
Anhydrous DMSO solution	Quality Biological, Inc. Gaithersburg, MD	1×
4-Hydroxy-TEMPO (4HT) solution	Sigma Aldrich, Saint Louis, MO	1×
Tetramethylethylenediamine (TEMED)	Thermo Fisher Scientific, Rockford, IL	10%
Ammonium persulfate (APS)	Sigma Aldrich, Saint Louis, MO	10%
Sodium Acrylate	Sigma Aldrich, Saint Louis, MO	38%
Acrylamide	Bio-Rad, Hercules, CA	40%
N,N- Methylenebisacrylamide	Sigma Aldrich, Saint Louis, MO	2%
Sodium Chloride	Quality Biological, Inc. Gaithersburg, MD	5 M
Ethylenediaminetetraacetic acid	Quality Biological, Inc. Gaithersburg, MD	0.5 M
Tris Cl	Quality Biological, Inc. Gaithersburg, MD	1 M

2.2 Protocol

2.2.1 Tissue Preparation

C57 BALB/c mice were transcardially perfused with a mixture of BriteVu™ (Scarlet Imaging, LCC; Murray, UT, USA) and Galbumin™-Rhodamine B (BioPAL Inc., MA) solution, or Tomato lectin-Texas Red (Vector Laboratories, Burlingame, CA) solution, followed by fixation for 2-3 days in 10% buffered formalin at 4° C. Once the animal was fixed, the brain, muscle, kidneys, liver, and lungs were excised and placed in 10% buffered formalin (Sigma Aldrich, Saint Louis, MO) overnight. Following fixation, tissues were transferred to a 30% sucrose cryoprotectant solution (Sigma Aldrich, Saint Louis, MO) and incubated overnight at 4° C and then frozen in liquid nitrogen (Sigma Aldrich, Saint Louis, MO). Excess sucrose was removed from the sample before it was placed in a cryomold and embedded in the optimal cutting medium (OCT, Sakura Finetek, Torrance, CA) and placed on a pan floating on liquid nitrogen so that it gradually froze over 15 minutes. The sample was then transferred to a cryostat to allow it to acclimatize to the temperature in the cryostat chamber (-22° C) for 30-60 minutes before slicing it into sections that ranged from 10-100 μm for immunofluorescence staining and subsequent microscopy.

2.2.2 Immunofluorescence staining

Immunofluorescence staining was performed on tissue sections to detect the presence of laminin and α-SMA on the vasculature. The sections were first washed in a PBS solution for 15 minutes and then permeabilized in PBST solution (PBS containing 0.5% Tween 20) for 15 minutes on an orbital shaker at 30 rpm. Once permeabilized, the samples were incubated in carbo-free

blocking solution (Vector Labs, Burlingame, MA) for 1 hour at room temperature. Blocking prevented non-specific binding of antibodies to the tissue, thus reducing background due to non-specific staining. Subsequently, the sections were incubated overnight in 150 µl of the pre-conjugated primary anti-α-SMA-FITC (1:100 dilution) and primary anti-laminin (1:200 dilution) antibody. The incubation period was directly proportional to the thickness of the tissue sections (1 night/10 µm). Next, the sections were rinsed multiple times in PBS solution. For the pre-conjugated antibody, the sections were immediately transferred onto a slide, counterstained with DAPI for 1-3 minutes, mounted in aqueous mounting medium and cover slipped. For the unconjugated antibody, a two-step labeling procedure was followed. Once the anti-laminin antibody was rinsed, the sections were incubated with goat anti-rabbit Cy-3 secondary antibody for 3 hours. After the secondary antibody was rinsed off with PBS, the counterstaining and mounting steps were repeated for these tissue sections. Multiple fields of each sample were imaged using a Zeiss 710 NLO multiphoton microscope equipped with appropriate filter sets (please see section **2.4.2**).

2.2.3 Gel Preparation for Sample Expansion

To physically expand the tissue, expansion microscopy requires the sample to be embedded in a dense hydrogel synthesized evenly throughout the specimen, which undergoes isotropic expansion when immersed in water.

Once the pre-expansion samples were imaged, they were prepared for the expansion process. The slides were incubated in PBS for 2 hours to remove the coverslip with ease. The samples were removed from the slide and rinsed in PBS for 10 minutes to start the first step of

expansion, i.e. gelation. The following solutions were prepared beforehand: AcX /DMSO solution, Stock X, 4HT, TEMED and APS.

1. The tissue was incubated in the AcX solution overnight at room temperature.

2. While the sample was incubating in AcX, a gelation chamber was constructed, by placing two No. 1.5 coverslips on the edges of the slide. The coverslips were kept in place with the help of superglue. The coverslips were then wrapped using parafilm. The parafilm ensured the chamber was airtight, preventing leakage of the gel solution from the edges when the lid (i.e. coverslip) was placed over the chamber.

3. Once the samples were done incubating in AcX solution, they were washed twice in PBS for 15 mins at a time.

4. The gelling solution was freshly prepared each time by adding Stock X, 4HT solution, TEMED and APS together in this specific order at a volumetric ratio of 47:1:1:1.

5. 100 µl of the gelling solution was placed in the chamber onto which the tissue sample was transferred carefully using a paint brush, taking care to ensure there were no folds in the tissue section. Once the lid was placed on the slide and air bubbles removed, the chamber was kept in the dark at 4^{o} C for 30 minutes. After this initial incubation, the chamber was transferred to a 37^{o} C incubator for 1-2 hours depending on the thickness of the tissue section, for polymerization. Care was exercised to ensure that the chamber was not tilted or shaken during the gelation process.

2.2.4 Digestion

After the chamber was removed from the incubator, the lid was gently separated from the it. Using a fine paint brush, the gel was transferred into a container of digestion buffer in which it incubated overnight at room temperature in the dark.

2.2.5 Expansion and Storage

The digested gel was trimmed to a reasonable size for ease of handling. When the sample was ready to be imaged, the gel was immersed in water for 10 minutes. This was repeated three times with fresh water for a total of 30 minutes. At this juncture the sample is optically clear, completely expanded, and ready for imaging. In case the samples do not need to be imaged immediately after gelation, the gel embedded samples can be stored in PBS in the dark at 4^{o}C, after which they can be expanded.

2.3 Vascular Labels

2.3.1 Structure of Blood Vessels

Blood vessels form a complex and organized network in organisms to facilitate the transport of blood cells, oxygen, and other nutrients throughout their body, while simultaneously removing the waste and carbon dioxide expended by their organs [46].

The vascular network consists of three major types of blood vessels: arteries, capillaries, and veins. Arteries deliver the blood from the heart to the organs by branching into smaller vascular

structures called arterioles which finally form capillaries that are 5-10 μm in diameter and are the primary site of exchange for nutrients like oxygen. Capillaries eventually merge to form venules. Venules are 7 μm to 35 μm in diameter and connect the capillaries to the veins that transport the carbon dioxide rich blood back to the heart [46][47].

Structurally, arteries and veins can be deconstructed into three layers which surround the lumen. The tunica intima, the innermost and thinnest layer consisting of endothelial cells which is supported by connective tissue. The second layer, tunica media, is made up of smooth muscle actin, elastic fibers, and connective tissue. Being one of the thickest layers in the vessel, it provides structural support, the smooth muscle cells impart vasoreactivity, i.e. they contract or relax blood vessels based on signals from the autonomic nervous system and the elastic fibers maintain the elasticity of the vessel by allowing it to expand and contract, thereby controlling the flow of blood. Finally, the outermost layer is the tunica externa or adventitia that is composed of connective tissue fiber. Due to their minimal thickness, capillaries do not need much structural support and are only made up of a single layer of endothelial cells [47].

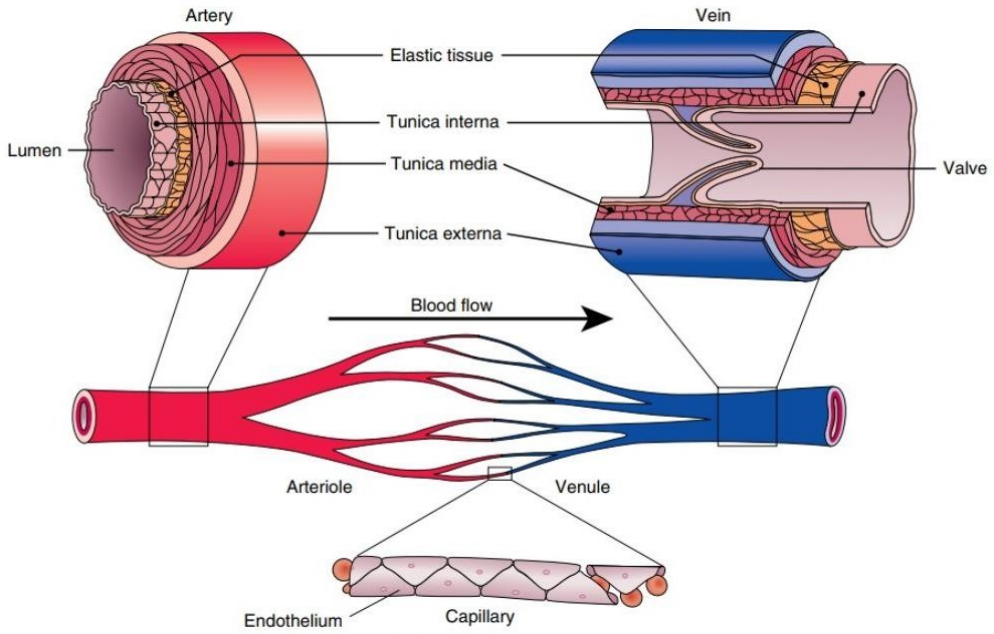

Fig 7. Typical structure of an artery, vein and capillary. The image labels the different layers of an artery, vein and capillary. The arteries and veins are divided into elastic tissue, tunica interna, tunica media and tunica externa which envelop the lumen. The arteries and veins branch into arterioles and venules which further diverge into capillaries, which transport blood and other nutrients in organs to and from the heart [47].

The primary antibodies were chosen based on the different antigens they bound to blood vessels. The specificity of the binding mechanism between the antibodies and their antigen is an advantageous way to selectively identify proteins in the endothelial or smooth muscle cells in a tissue section.

2.3.2 Tomato Lectin

Tomato lectin is a carbohydrate that binds to the luminal surface of endothelial cells and the N-glycan glycoproteins associated with the endothelial cells. These surface glycoproteins act as binding sites for a variety of endogenous molecules and the injected tomato lectin may have to compete with these molecules to access the binding site. This is commonly employed as an intravascular tag for blood vessels in preclinical studies [48]. Tomato lectin preconjugated to the

fluorophore Texas Red (Vector Laboratories, Burlingame, CA) was administered intravenously to the animal at a concentration of 20 μg/ml. Once the animal was euthanized, it was placed in 10% buffered formalin for two days to fix the organs before harvesting them.

2.3.4 BriteVu

BriteVu™ solution (Scarlet Imaging, LCC; Murray, UT, USA) is a radiodense intravascular contrast agent used to visualize the vasculature using x-ray CT. It is transcardially perfused into the animal after heparinized saline has been used to flush out the blood, followed immediately by freshly prepared solution according to the manufacturer instructions. Once the animal is perfused, it is incubated overnight at 4° C, to enable polymerization [49]. For concurrent fluorescent imaging, a Rhodamine B conjugated MRI contrast agent, Galbumin™-Rhodamine B (BioPAL Inc., MA) was added to the BriteVu solution prior to perfusion. Rhodamine B has an excitation maximum of 556 nm and a maximal emission wavelength of 627 nm [50].

2.3.4 Laminin

Vascular basement membrane (BM) is a fibrous, extracellular matrix that envelopes endothelial cells. Communication between the BM and the endothelial cells is integral to maintaining the structure and function of the vessel walls [51]. Laminins are one of the main components of the vascular basement membrane. They are heterotrimeric glycoproteins consisting of α, β, and γ chains. There are 15 different isoforms of laminin that have been discovered based on the placement of these chains. Anti-laminin antibodies bind to these laminin structures in the

vascular basement membrane [52]. An unconjugated, anti-laminin (Sigma Aldrich, Saint Louis, MO) primary antibody was used at 1:200 dilution with overnight incubation at room temperature. A goat anti-rabbit Cy-3 was used as the secondary antibody at a 1:100 dilution.

2.3.5 Alpha-Smooth Muscle Actin

Found in between the endothelial cells and connective fibers, smooth muscle is present to maintain the structural integrity and vasoreactivity of the vasculature, as described in section **2.3.1.** Smooth muscle is found more frequently in the larger blood vessels since they require more structural support than the finer capillaries [53]. Sections were incubated in 1:100 dilution of α-Smooth Muscle Actin (Sigma Aldrich, Saint Louis, MO) pre-conjugated to the fluorophore FITC. The sections were incubated overnight at room temperature.

2.3.6 Counterstains

Some sections were counterstained with 4′,6-diamidino-2-phenylindole, dihydrochloride (DAPI, Thermo Fisher Scientific, Richmond, IL) and anti GFAP-Alexa Fluor 488 (Biolegend, Dedham, MA) to distinguish the nuclei and astrocytes, respectively. DAPI is a fluorophore which binds to the AT regions in the minor curve of dsDNA and is therefore used as a nuclear counterstain. DAPI is excited between 358-461 nm and fluoresces in the blue (~490–450 nm) [54] region of the visible spectrum. GFAP is a member of the family of intermediate filaments. They form networks around the glial cells to support and strengthen their structure. Multiple GFAP proteins bind together to form astroglial cells or astrocytes. These cells play many crucial roles in

maintaining and repairing a variety of cells in the central nervous system. GFAP conjugated to Alexa Fluor 488 that is excited at 495 nm and fluoresces in ~560-520 [55] part of the visible spectrum was used for this study.

2.4 Fluorescence Imaging

2.4.1 Principle of Fluorescence Microscopy

Fluorescence is a physical phenomenon wherein a material emits light as the result of absorbing light of a shorter wavelength in the form of photons. The difference in incident and emitted wavelength was called the Stokes shift after physicist George Gabriel Stokes [56][57]. After absorption of photons, the electrons in the ground state of the substance shift to the higher energy level. At this level, the electrons are very unstable and dissipate their energy through internal conversion and vibrational relaxation, falling to the first excited state. The wavelength of the emitted light is inversely proportional to energy according to: $E = hc/\lambda$, where E = energy, h = Planck's constant, ν = frequency, c = the speed of light in vacuum, and λ = wavelength. Therefore, the loss in energy due to the Stokes shift results in the emission of a longer wavelength photon. This is represented pictorially by the Jablonski energy diagram shown in **Fig 8** [58].

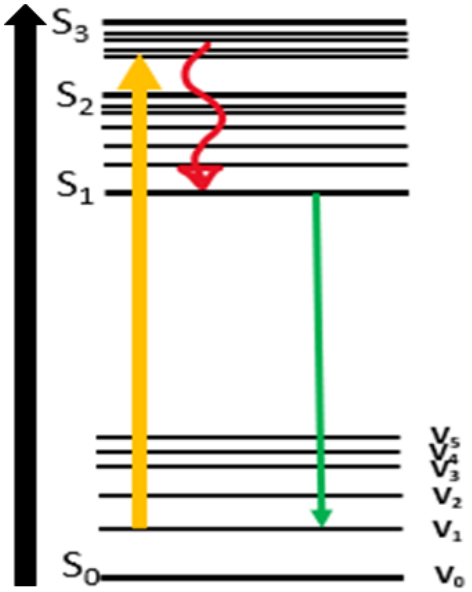

Fig 8. Jablonski Energy Diagram. The diagram shows the shift of electrons from ground state to higher energy level where they are highly unstable. To achieve stability, they dissipate energy falling to the first excited state. This loss in energy results in the emission of a photon with longer wavelength.

2.4.2 Confocal microscopy

Confocal microscopy is a widely used optical imaging technique. Unlike a compound light or fluorescence microscope that captures light from multiple focal planes to create a single two-dimensional image, confocal microscopes acquire images by focusing light on a single point within a defined focal plane via a spatial pinhole, eliminating scattered light from non-focal planes. This significantly reduces image distortion and improves resolution when imaging thick tissue samples. Point-by-point scanning of two-dimensional images at varying depths can be captured from multiple planes and reconstructed into a three-dimensional image of the sample. Laser scanning microscopy is a confocal technique that serially images a sample using various laser excitation lines and emission filters, facilitating detailed fluorescence imaging [59].

2.4.3 Two-photon excitation (2PE) microscopy

2PE is a recently developed microscopy technique based on a nonlinear optical process that uses two low-energy photons from the same laser. The molecule to be imaged absorbs the identical photons simultaneously. The intensity is highest in the vicinity of the focus and drops off quadratically with distance above and below reducing photodamage to regions surrounding the focal point. Therefore, fluorophores are excited in a small focal region. The excitation wavelengths used in 2PE microscopy, are in the deep red and near IR (~700-1200 nm) range and penetrate tissue better than the visible wavelengths (~390-700 nm) used in single-photon microscopy techniques. 2PE offers comparable contrast and resolution to confocal microscopes without the pinhole [60].

2.4.4 Image Acquisition

Pre- and post-expansion images of the tissues were acquired on a Zeiss LSM 710 NLO using a W Plan-APOCHROMAT 20×/1.0 water immersion objective. Multiple fields of view (FOV) were acquired from each sample using UV (355 nm), HeNe (458/488/514 nm) and argon (543 nm, 561 nm, 594 nm, 633 nm) lasers [61]. Laser excitation wavelengths were selected based on fluorophores used in the immunofluorescence staining procedure (**Table 2.2**).

Table 2.2: List of fluorophores used in this study.

FLUOROPHORE	CHEMICAL NAME	ABSORPTION MAXIMA (λ_{abs})	EMISSION MAXIMA (λ_{em})
Alexa-Fluor 488 [20]	-	495 nm	519 nm
FITC [20]	Fluorescein isothiocyanate	494 nm	518 nm
Texas Red [20]	-	596 nm	615 nm
Cy-3[20]	Cyanine	554 nm	568 nm
DAPI [20]	4′,6-diamidino-2 phenylindole, dihydrochloride	350 nm	470 nm

2.5 Image Preprocessing

Vessels were segmented from the acquired z-stack images using the interactive microscopy image analysis software IMARIS® 9.5.1 (Oxford Instruments, Belfast, UK). First, the 3D rendered image was preprocessed using IMARIS®'s inbuilt image processing menu. The menu provides various smoothing, thresholding and contrast functions. A combination of gaussian filter, background subtraction, and normalization functions was optimized for smoothing, thresholding, and contrast adjustment, respectively. The gaussian filter smoothens the image by removing structures smaller than the manually adjustable filter width. The process preserves the total image intensity while suppressing noise evenly across it. The background subtraction function defines the background at each voxel using the gaussian filter width and performs baseline subtraction of the background to eliminate any non-uniformities in the background. The manually entered baseline value is subtracted from the intensity of each voxel in the image, if the result is positive,

that value is set as the new intensity of the voxel, else if the result is negative, the intensity of that voxel is set to zero. And finally, the normalize layer function adjusts the brightness and contrast of each individual z-slice to a uniform range. The algorithm computes mean and standard deviation for the entire z-stack and then repeats the calculations for each individual slice. The intensity of each section is then adjusted to match the overall mean and standard deviation by linear transformation.

Once the images were preprocessed, they were opened in *surpass view*. In this view an object toolbar is visible on the screen, which offers tools to segment different cellular structures. For vessel extraction the *FilamentTracer* tool was used. The *FilamentTracer* feature was created to segment, edit, display and measure neuronal structures like dendrites and filaments, however, they have also been used successfully for segmentation of blood vessels. The creation wizard window acts as a user interface element, sequentially guiding the user through all the steps required to process the data **(Fig 9 A and B)** [62].

1. The First window presents the user with two algorithms to automatically create filaments. These options were *AutoPath* and *Thresholding*. We selected the *AutoPath Algorithm* because this method segments the vessels based on the local intensity contrast **(Fig 9 C)**.

2. In the second window, the channel which needs to be processed is selected, and each channel was segmented separately. Vessels were tagged with red fluorophores (e.g. Texas Red, Cy3 and Rhodamine B), therefore the red channel was selected to be segmented first. The checkbox provided for the calculation of the diameter of each filament was also selected. Also, in the third window, the starting point diameter (SPD) and end point diameter (EPD) were specified.

These limits act as the upper and lower thresholds for the diameter of vessels to be segmented and were selected based on the thickness of vessels **(Fig 9 D)**.

3. The third window displays histograms for SPD and EPD along with their thresholds. The thresholds can be manually adjusted, and the update viewed in the display area. The *AutoPath Algorithm* generates starting points from where the vessels branch out and places seeds along the vessel based on local intensity contrast as per the threshold specified in the histogram. The box specifying removal of seed points near the starting point is unchecked, and the *Remove Disconnected Segments* option was selected. These filters improve the accuracy of the filament tracing while eliminating the regions of high background noise and low signal regions by setting the gap length to determine which vessels were disconnected **(Fig 9 E)**.

4. The fourth window appears when *Remove Disconnected Segments* is selected. This window provides a histogram to manually adjust the vessels segmentation selected by local thresholding **(Fig 9 F)**.

5. The final step before segmentation is the selection of the algorithm for measuring the vessel diameter. IMARIS® offers two methods for calculating the diameter: the shortest distance from a distance map or the approximate circle of a cross-sectional area. In the first method, the seed point acts as the center of the vessel and the closest boundary from that point is considered the diameter. In the second method, the diameter gets calculated from a circular cross section area around the seed point, the value of which was determined manually using a histogram and adjusting the threshold. Either of the two methods can be selected based on which one shows better segmentation of vessel. The shortest distance works better when there are fewer starting points and more seeds,

while the approximate cross-sectional area option is preferred when a large variation is seen in the thickness of vessels in the same FOV **(Fig 9 G)**.

6. The final segmented output can be seen overlain on the display area while the statistical data is seen in the final window **(Fig 9 G)**.

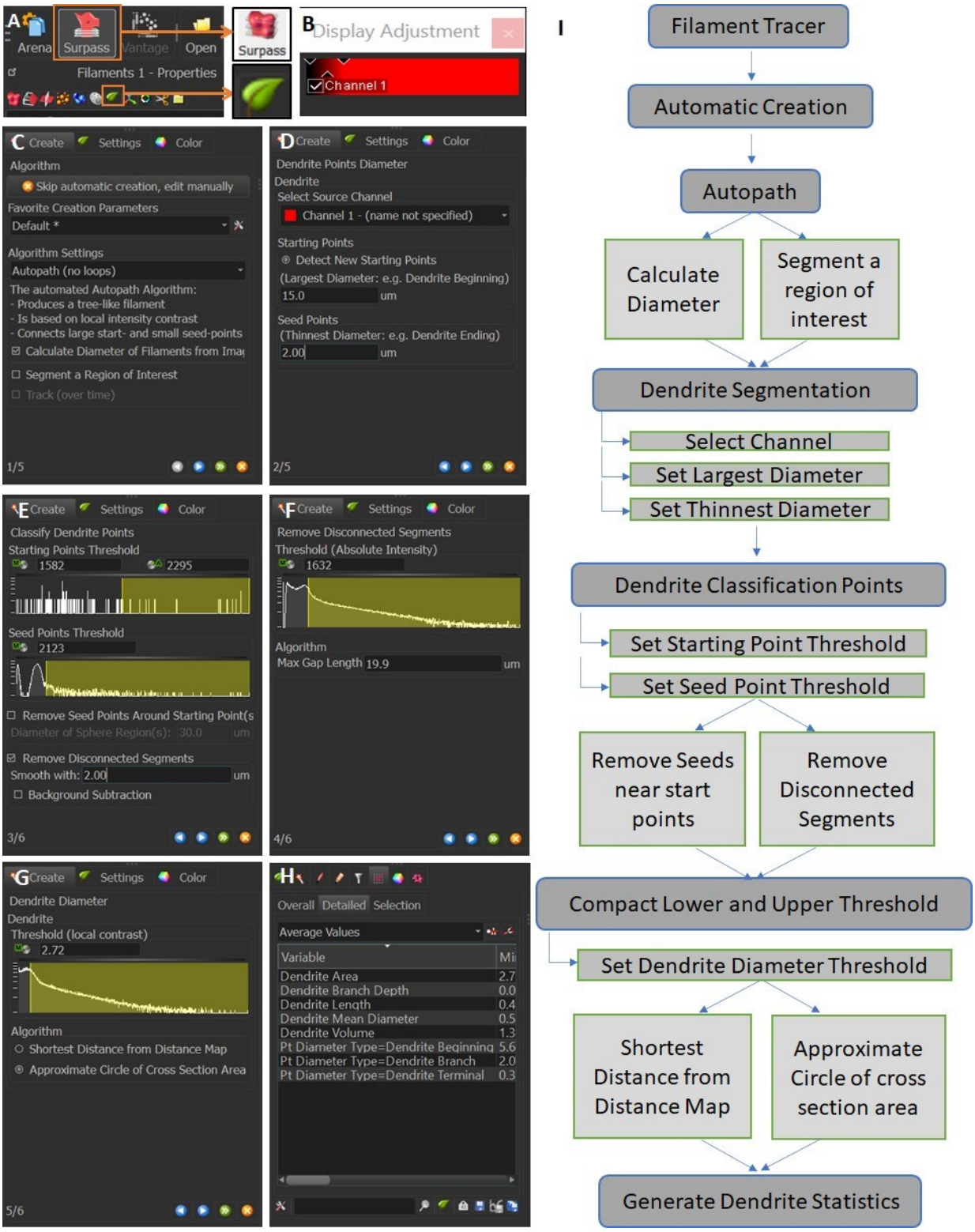

Fig 9. (Left) Workflow of *FilamentTracer* tool in IMARIS®. (Right) Flowchart illustrating the vessel segmentation pipeline followed in IMARIS®.

2.6 Quantitative Analysis

IMARIS® processes the final segmented data to generate summary statistics of the following variables: Dendrite Area, Dendrite Volume, Dendrite branch Depth, Dendrite Mean Diameter. Mean data values were used for all analyses. For multiple FOV of the same sample, a two-tailed paired *t*-test was used to determine if there was a significant difference in vessel diameter and vascular volume between the pre- and post-expansion groups. For analyzing the differences in vessel diameter and vascular volume pre- and post-expansion across multiple samples, a one-tail paired *t-test* was performed (p-values ≤ 0.05 were considered significant).

CHAPTER 3

3. Results

3.1 Validation of expansion

The results of statistical analysis methods described in Ch 3 are elaborated on in this chapter. For paired and unpaired *t-tests* the null hypothesis (H_0) tested was that there was no significant difference in vascular architecture after tissue expansion. Hence, the alternative hypothesis (H_1) was that there was a change in the vascular architecture after the expansion process. The *t-tests* were conducted on pre- and post-expansion values of morphological parameters such as: mean vessel diameter, mean vessel area, and mean vessel volume computed using the IMARIS® software. The changes in mean intensity of fluorescence of the samples before and after expansion were also measured using the Fiji software.

3.2 Vascular Architecture for Brain Tissue

3.3.1 Pre-expansion

The morphological parameters for the vasculature extracted from brain tissue before expansion are summarized in **Tables 3.1** and **3.2**.

Table 3.1 –Mean values for vessel diameter, vessel volume, vessel area and vessel length for three (T)Lectin – Texas Red labeled coronal mouse brain sections (M1-M3) from two or more FOV.

Morphological Parameters	M1	M2	M3
Mean vessel diameter ± Std Dev (μm)	3.35 ± *1.71*	4.01 ± *1.34*	4.38 ±*1.01*
Mean vessel volume ± Std Dev $(\mu m)^3$	220.10 ± *193.23*	328.00 ± *388.16*	267.96 ± *251.20*
Mean vessel area ± Std Dev $(\mu m)^2$	183.93 ± *167.37*	295.79 ± *321.41*	239.96 ± 217.19
Mean vessel length ± Std Dev (μm)	18.52 ± *16.84*	22.37 ± *24.76*	17.87 ± *19.36*

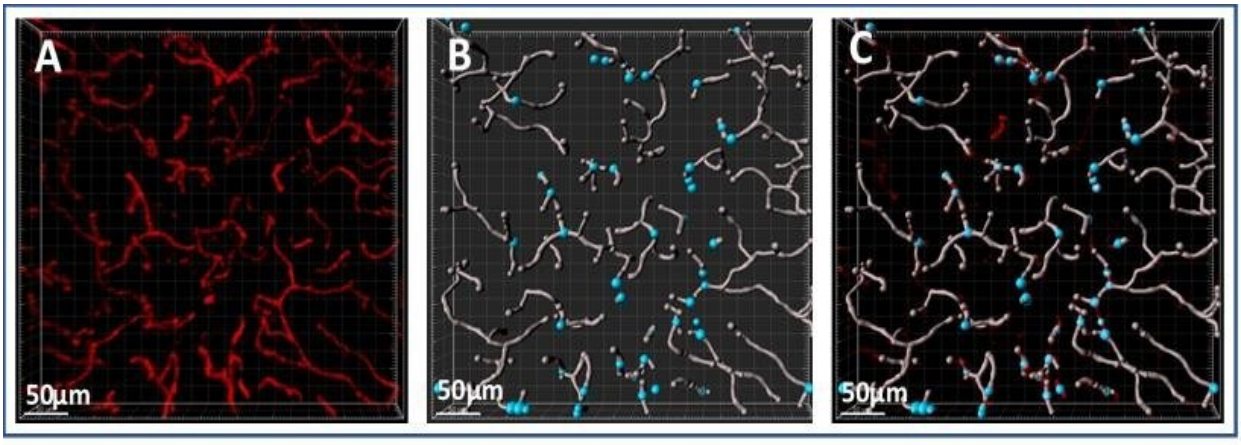

Fig 10. Results of preprocessing and segmentation of (T)Lectin-Tx Red labeled vessels in brain vasculature of pre-expansion mouse M1: (A) Rendering of the preprocessed confocal image of a FOV of (T)Lectin-TxRed stained vessels from mouse M1 using Fiji software with Gaussian Blur = 2.0μm. (B) Segmentation of vessels (grey) in (A) using the *FilamentTracer* tool from IMARIS® which also computes the morphological parameters. The blue spheres indicate starting points for identifying vessel segments created by the IMARIS® algorithm (see section 2.5 for details). (C) Overlay of the results of preprocessed image (A) (red channel) and vessel segmentation (B) (gray channel) to assess the quality of segmentation.

Table 3.2 – Mean values for vessel diameter, vessel volume, vessel area and vessel length for two anti-Laminin Cy3 antibody labeled coronal mouse (M1 and M2) brain sections from two or more FOV.

Morphological Parameters	M1	M2
Mean vessel diameter ± Std Dev (μm)	8.28 ± *2.59*	10.11 ± *2.85*
Mean vessel volume ± Std Dev (μm)^3	939.05 ± *854.50*	*2324.80 ± 2096.12*
Mean vessel area ± Std Dev (μm)^2	488.41 ± *433.24*	10697 ± *989.63*
Mean vessel length ± Std Dev (μm)	37.55 ± *19.56*	31.96 ± *39.91*

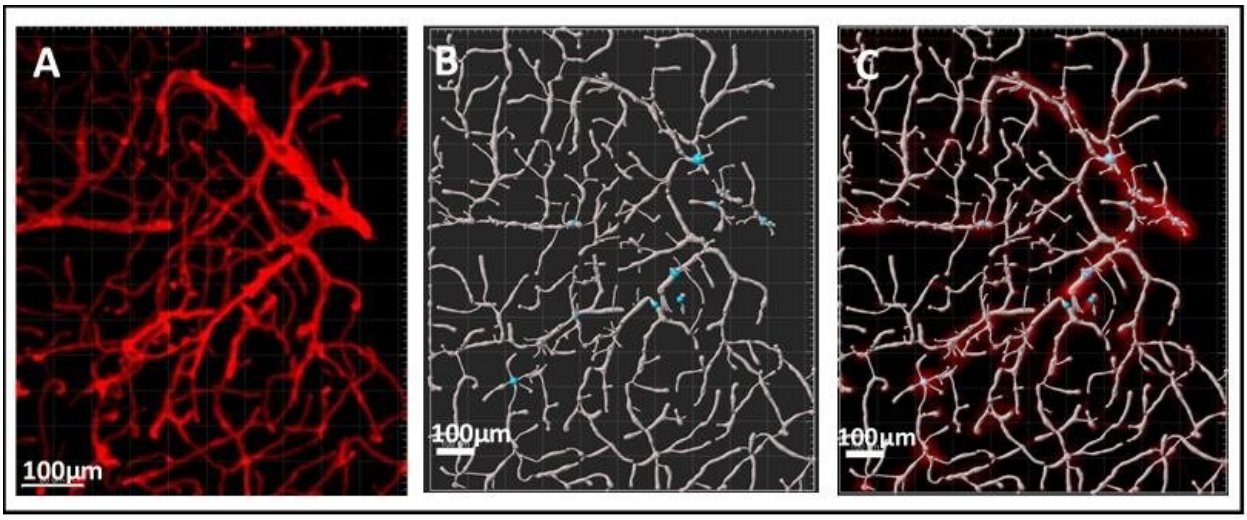

Fig 11. Results of preprocessing and segmentation of anti-Laminin Cy 3 labeled vessels in brain vasculature of pre-expansion mouse M1: (A) Volume rendering of the preprocessed confocal image of a FOV of vessels from mouse M1 using preprocessing tools in IMARIS® with Gaussian filter = 1.0μm, background subtraction = 106 μm. (B) Segmentation of vessels (grey) in (A) using the *FilamentTracer* tool from IMARIS®. The blue spheres indicate the starting points for identifying vessel segments created by the IMARIS® algorithm (see section 2.5 for details). (C) Overlay of the results of preprocessed image (A) (red channel) and vessel segmentation (B) (gray channel) to assess quality of segmentation.

3.3.2 Post- Expansion

The morphological parameters for vasculature extracted from brain tissues post-expansion are summarized in **Tables 3.3** and **3.4**.

Table 3.3 – Mean values for vessel diameter, vessel volume, vessel area and vessel length of three (T)Lectin – Texas Red labeled coronal mouse (M1-M3) brain sections from two or more FOV post-expansion.

Morphological Parameters	M1	M2	M3
Mean vessel diameter ± Std Dev (μm)	8.53 ± *2.58*	6.94 ± *1.51*	10.03 ± *3.74*
Mean vessel volume ± Std Dev $(\mu m)^3$	939.05 ± *847.80*	1134.17 ± *1164.23*	1518.04± *1301.22*
Mean vessel area ± Std Dev $(\mu m)^2$	488.5 ± *429.84*	1055.09 ± *1423.16*	726.56 ± *605.65*
Mean vessel length ± Std Dev (μm)	15.59 ± *19.41*	47.62 ± *57.33*	19.95 ± *33.69*

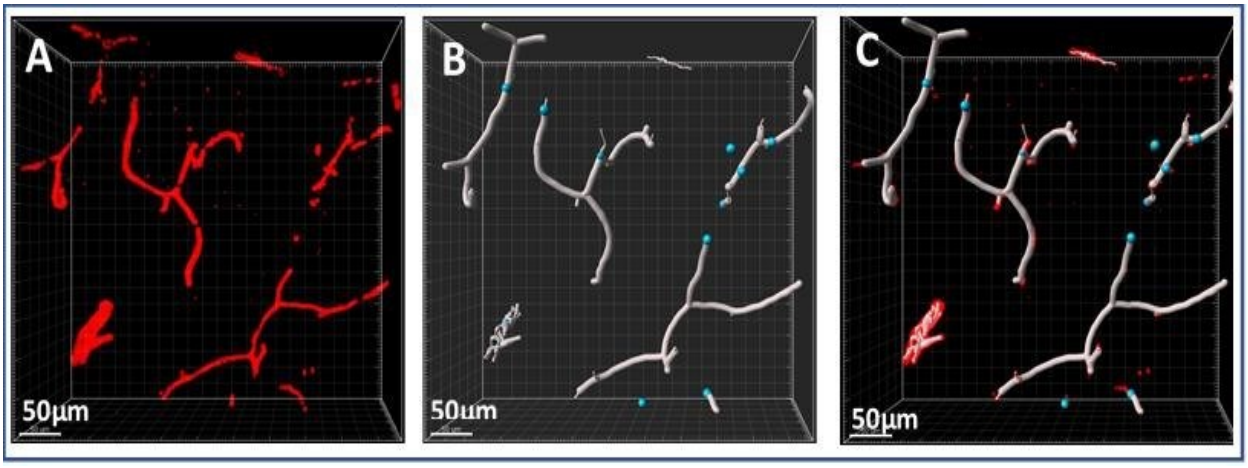

Fig 12. Results of preprocessing and segmentation of (T) Lectin-Tx Red labeled vessels in brain vasculature of post-expansion mouse M1 : (A) Volume rendering of preprocessed confocal image of a FOV of (T) Lectin-Tx Red stained vessels from mouse M1 using preprocessing tools in IMARIS® software, Linear Stretch, Gaussian filter = 1.0μm, background subtraction = 170μm. (B) Segmentation of vessels (grey) in (A) using the *FilamentTracer* tool from IMARIS®. The blue spheres indicate the starting points for identifying vessels created by the IMARIS® algorithm (see section 2.5 for details). (C) Overlay of the results of preprocessed image (A) (red channel) and vessel segmentation (B) (grey channel) to assess quality of segmentation.

Table 3.4 –Mean values for vessel diameter, vessel volume, vessel area and vessel length for two anti-Laminin Cy3 antibody labeled coronal mouse (M1-M2) brain sections from two or more FOV pre-expansion.

Morphological Parameters	M1	M2
Mean vessel diameter ± Std Dev (μm)	13.34 ± *3.61*	14.49 ± *4.06*
Mean vessel volume ± Std Dev (μm)^3	6217.96 ± *4871.65*	6899.84 ± *5580.41*
Mean vessel area ± Std Dev (μm)^2	1987.71 ± *1414.00*	2124.39 ± *1589.52*
Mean vessel length ± Std Dev (μm)	42.12 ± *39.11*	40.26 ± *48.44*

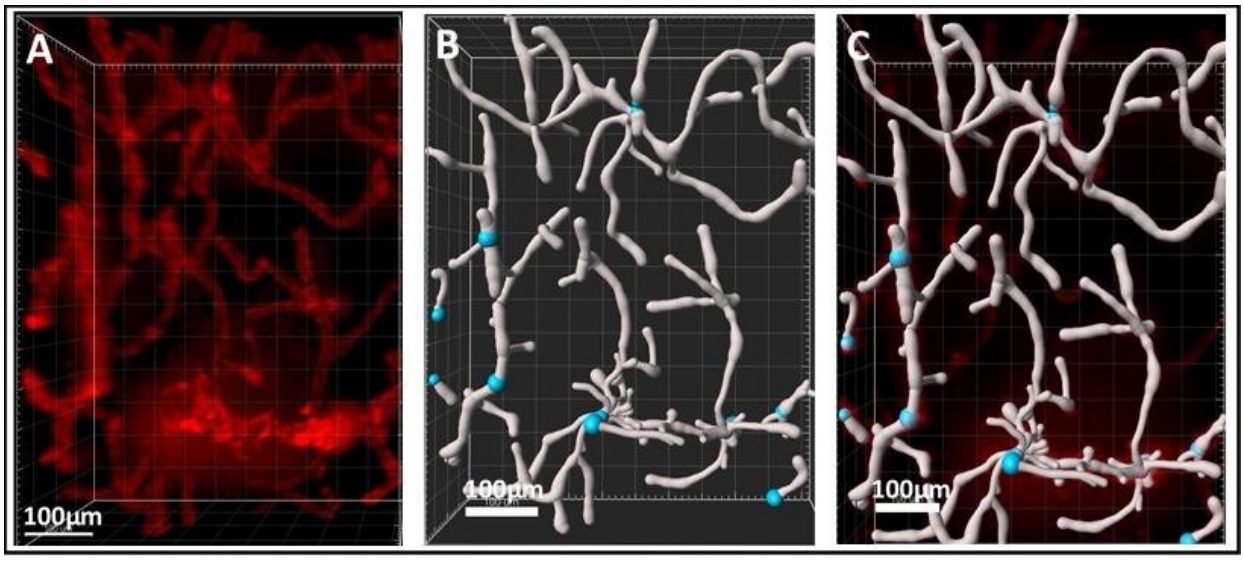

Fig 13. Results of preprocessing and segmentation of anti-Laminin Cy 3 labeled vessels in brain vasculature of post-expansion mouse M1 based on explanation given in Fig.5: (A) Rendering of the preprocessed confocal image of a FOV of anti-Laminin Cy3 labeled vessels from mouse M1 using preprocessing tools in IMARIS® with Threshold Cutoff = 30.4, Gaussian filter = 2.0μm and background subtraction = 78μm. (B) Segmentation of vessels (grey channel) in (A) using the *FilamentTracer* tool from IMARIS® which computes the morphological parameters. The blue spheres indicate starting points for identifying vessel segments created by the IMARIS® algorithm (see section 2.5 for details). (C) Overlay of the results of preprocessed image (A) (red channel) and vessel segmentation B to assess quality of segmentation.

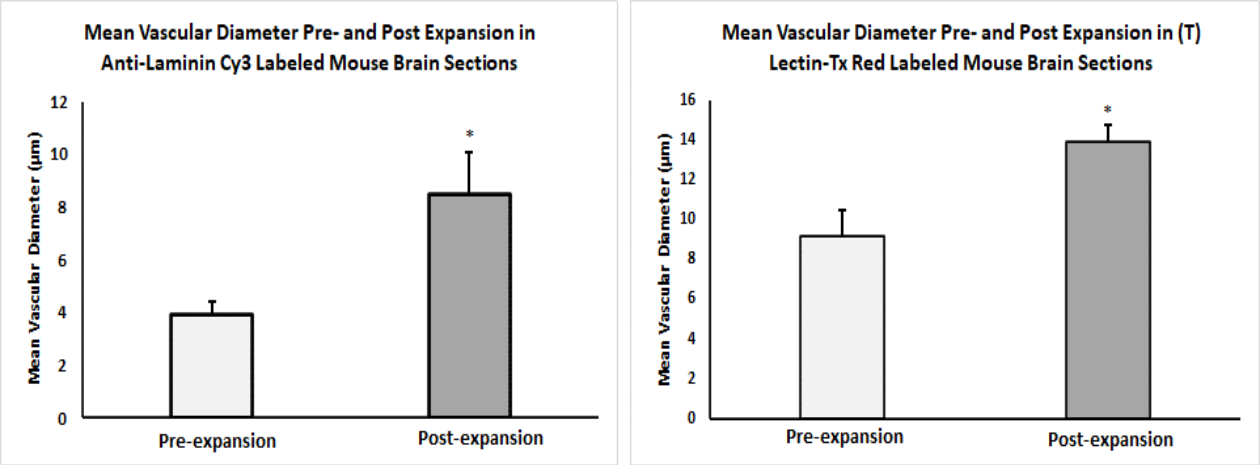

Fig 14. Comparison of mean vessel diameter across multiple samples pre-and post-expansion. (A) A 4.7 µm increase is observed between pre-expansion (9.12µm) and post-expansion mean vessel diameter (13.91µm) for anti-Laminin Cy3 labeled brain tissue. (B) For (T) Lectin-Tx Red labeled brain sections a 5.1µm increase is observed between pre-expansion (3.4µm) and post-expansion mean vessel diameter (8.5µm). *p-values<0.05. The error bars represent the standard deviation.

3.4 Vascular Architecture for Heart Tissue

3.4.1 Pre-Expansion

The morphological parameters for vasculature extracted from heart tissue before expansion are summarized in Table 3.5.

Table 3.5 – Mean values for vessel diameter, vessel volume, vessel area and vessel length of three (T) Lectin – Texas Red labeled coronal mouse (M1-M3) heart sections from two or more FOV pre-expansion.

Morphological Parameters	M1	M2	M3
Mean vessel diameter ± Std Dev(µm)	7.90 ± *4.08*	4.20 ± *0.66*	5.19 ± *1.01*
Mean vessel volume ± Std Dev(µm)^3	1205.99 ± *1433.78*	934.42 ± *873.59*	572.57 ±*571.88*
Mean vessel area ± Std Dev(µm)^2	506.46 ± *412.64*	856.24 ± *775.41*	546.37 ± *570.12*
Mean vessel length ± Std Dev(µm)	17.61 ± 15.11	65.29 ± *59.24*	45.44 ± *48.57*

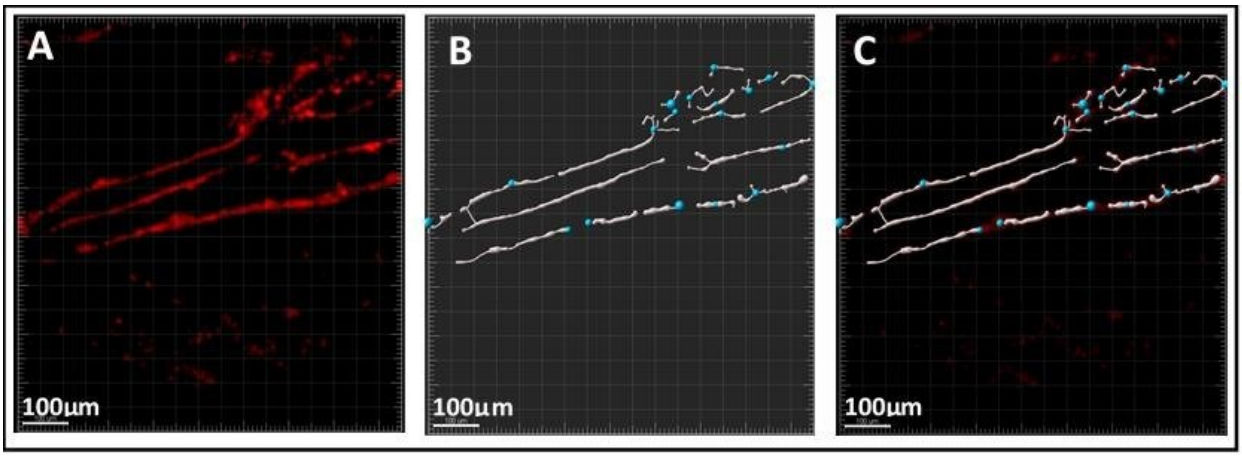

Fig 15. Results of preprocessing and segmentation of (T) Lectin-Tx Red labeled vessels in heart vasculature of pre-expansion mouse M1 : (A) Volume rendering of the preprocessed confocal image of a FOV of (T) Lectin-Tx Red stained vessels from mouse M1 using preprocessing tools in Fiji software, Gaussian blur = 1.0µm (B) Segmentation of vessels (grey) in (A) using the *FilamentTracer* tool from IMARIS® which also computes the morphological parameters. The blue spheres indicate starting points for identifying vessels segmented by the IMARIS® algorithm. (C) Overlay of the results of preprocessed image (A) (red channel) and vessel segmentation (B) (grey) to assess quality of segmentation.

3.4.2 Post-Expansion

The morphological parameters for vasculature extracted from brain tissue post expansion are summarized in Table 3.6

Table 3.6 – Mean values for vessel diameter, vessel volume, vessel area and vessel length of three (T) Lectin – Texas Red labeled coronal mouse (M1-M3) heart sections from two or more FOV post-expansion.

Morphological Parameters	M1	M2	M3
Mean vessel diameter ± Std Dev (µm)	3.27 ± *0.50*	2.76 ± *0.42*	2.75 ± *0.68*
Mean vessel volume ± Std Dev (µm)^3	129.02 ± *91.51*	83.60 ± *54.66*	73.29 + 69.24
Mean vessel area ± Std Dev (µm)^2	138.28 ± *85.48*	119.19 ± *132.73*	107.69 ± *95.33*
Mean vessel length ± Std Dev (µm)	13.36 ± *11.61*	14.13 ± *13.02*	13.02 ± *11.86*

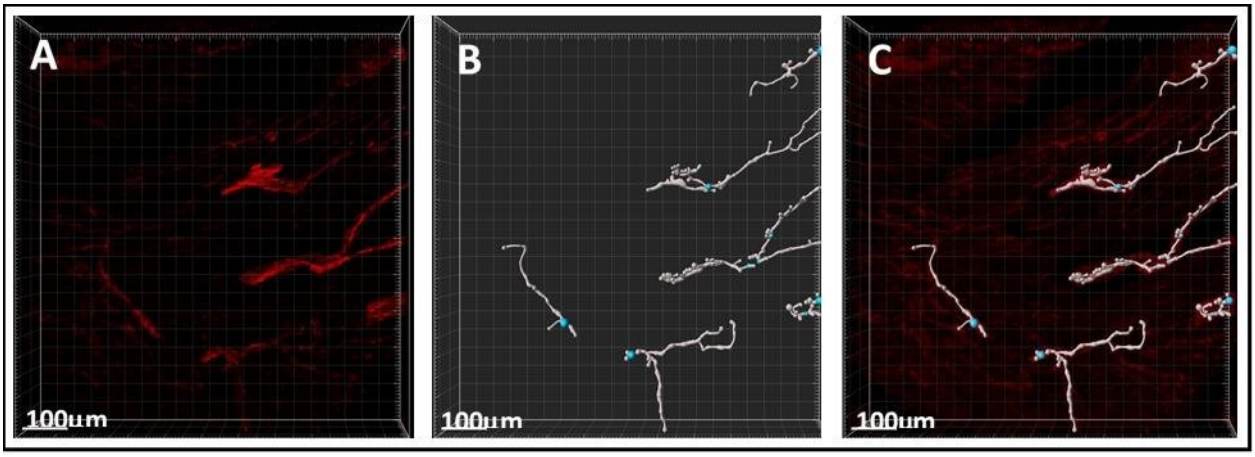

Fig 16. Results of preprocessing and segmentation of (T) Lectin-Tx Red labeled vessels in heart vasculature of post-expansion mouse M2 : (A) Rendering of the preprocessed confocal image of a FOV of (T) Lectin-Tx Red stained vessels from mouse M2 using preprocessing tools in IMARIS® software, Threshold Cutoff = 42.4, Gaussian filter = 2.0µm and background subtraction = 105µm (B) Segmentation of vessels (grey) in (A) using the *FilamentTracer* tool from IMARIS®. The blue spheres indicate starting points for identifying vessels created by the IMARIS® algorithm. (C) Overlay of the results of preprocessed image (A) (red channel) and vessel segmentation (B) (grey) to assess quality of segmentation.

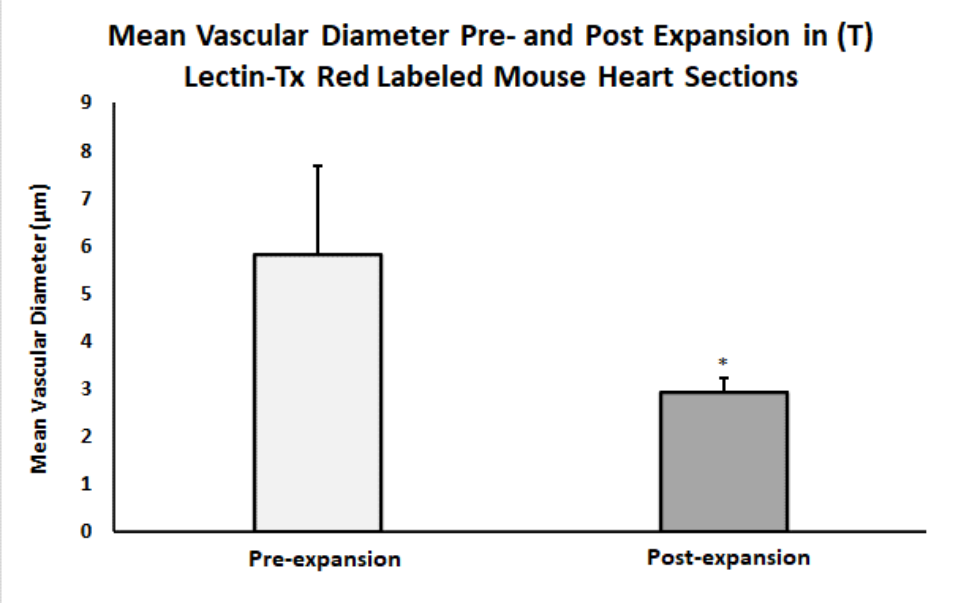

Fig 17. Comparison of mean vessel diameter across multiple samples pre-and post-expansion for (T) Lectin-Tx Red labeled heart sections. A 3.83µm decrease is observed between pre-expansion (6.76µm) and post-expansion mean vessel diameter (2.93µm). *p-values<0.05. The error bars represent the standard deviation.

3.5 Vascular Architecture for Liver Tissue

3.5.1 Pre-Expansion

The morphological parameters for vasculature extracted from liver tissue before expansion are displayed in Table 3.7

Table 3.7 – Mean values for vessel diameter, vessel volume, vessel area and vessel length of two tomato lectin – Texas Red labeled coronal mouse liver (M1-M2) sections from two or more FOV pre-expansion.

Morphological Parameters	M1	M2
Mean vessel diameter ± Std Dev (μm)	2.41 ± *0.53*	2.28 ± *0.35*
Mean vessel volume ± Std Dev (μm)^3	155.84 ± *36.17*	202.85 ± *36.66*
Mean vessel area ± Std Dev (μm)^2	331.49 ± *50.06*	387.82 ± *55.62*
Mean vessel length ± Std Dev (μm)	8.31 ± *7.59*	59.20 ± *9.46*

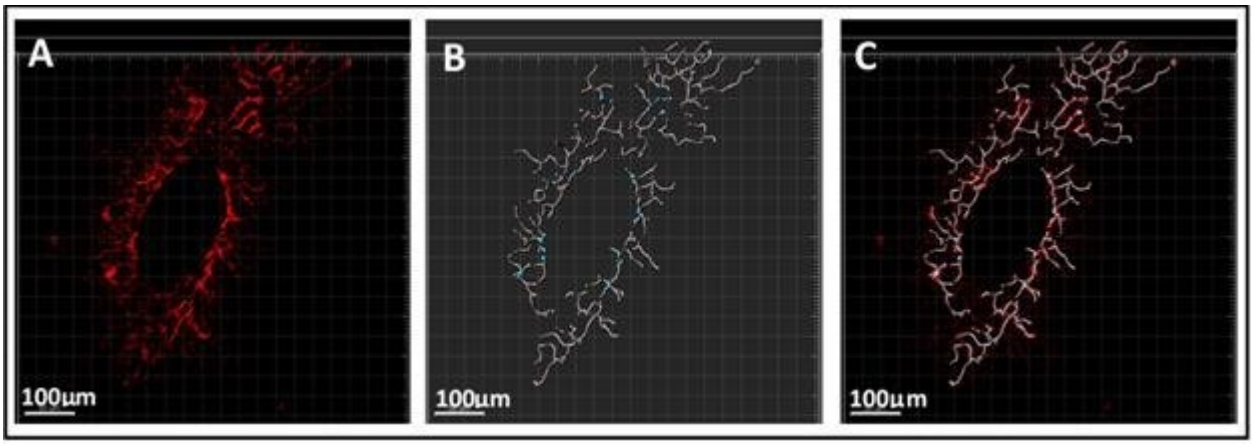

Fig 18. Results of preprocessing and segmentation of (T) Lectin-Tx Red labeled vessels in liver vasculature of ppre-expansion mouse M1 : (A) Rendering of preprocessed confocal image of a FOV of (T) Lectin-Tx Red stained vessels from mouse M1 using preprocessing tools in IMARIS® software, Threshold Cutoff = 24.4, Gaussian filter = 2.0μm and background subtraction = 124μm (B) Segmentation of vessels (grey) in (A) using the *FilamentTracer* tool from IMARIS® which also computes the morphological parameters. The blue spheres indicate starting points for identifying vessels created by the IMARIS® algorithm. (C) Overlay of the results of preprocessed image (A) (red channel) and vessel segmentation (B) (grey) to assess quality of segmentation.

3.5.2 Post-Expansion

The parameters for vasculature extracted from liver tissue before expansion are displayed in **Table 3.8.**

Table 3.8 – Mean values for vessel diameter, vessel volume, vessel area and vessel length of two (T) Lectin – Texas Red labeled coronal mouse (M1-M2) liver sections from two or more FOV post-expansion.

Morphological Parameters	M1	M2
Mean vessel diameter ± Std Dev (μm)	7.23 ± *1.34*	4.32 ± *0.36*
Mean vessel volume ± Std Dev (μm)^3	*1575.87 ± 1909.50*	367.8 ± *42.8*
Mean vessel area ± Std Dev (μm)^2	850.23 ± *1002.21*	592.9± *68.9*
Mean vessel length ± Std Dev (μm)	*36.06 ± 42.37*	30.01 ± *9.81*

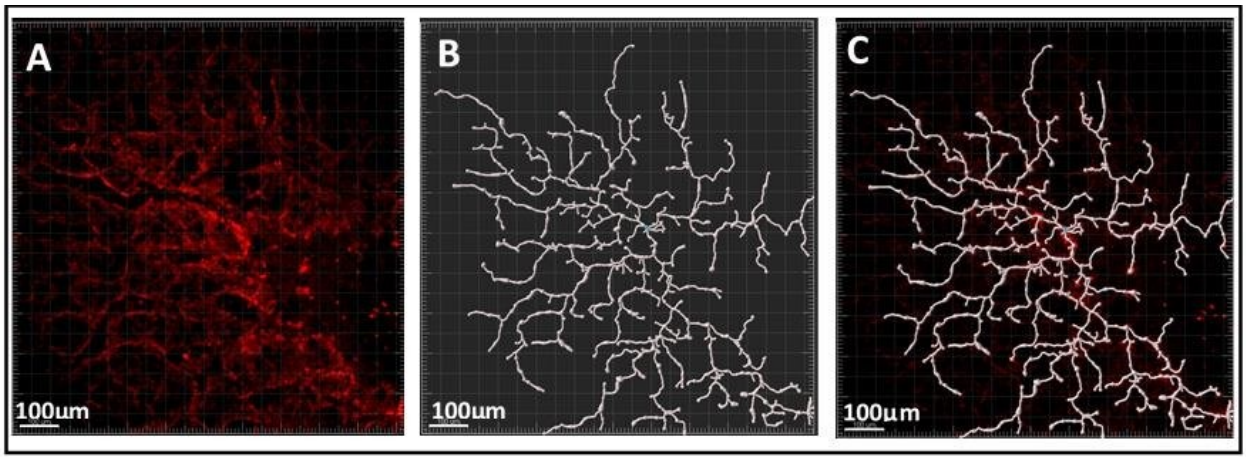

Fig 19. Results of preprocessing and segmentation of (T) Lectin-Tx Red labeled vessels in liver vasculature of post-expansion mouse M1 : (A) Rendering of the preprocessed confocal image of a FOV of (T) Lectin-Tx Red stained vessels from mouse M1 using preprocessing tools in IMARIS® software, Threshold Cutoff = 29.6, Gaussian filter = 2.0μm and background subtraction = 106μm (B) Segmentation of vessels (grey) in (A) using the *FilamentTracer* tool from IMARIS®. The blue spheres indicate starting points for identifying vessels segmented by the IMARIS® algorithm. (C) Overlay of the results of preprocessed image (A) (red channel) and vessel segmentation (B) (grey) to assess quality of segmentation.

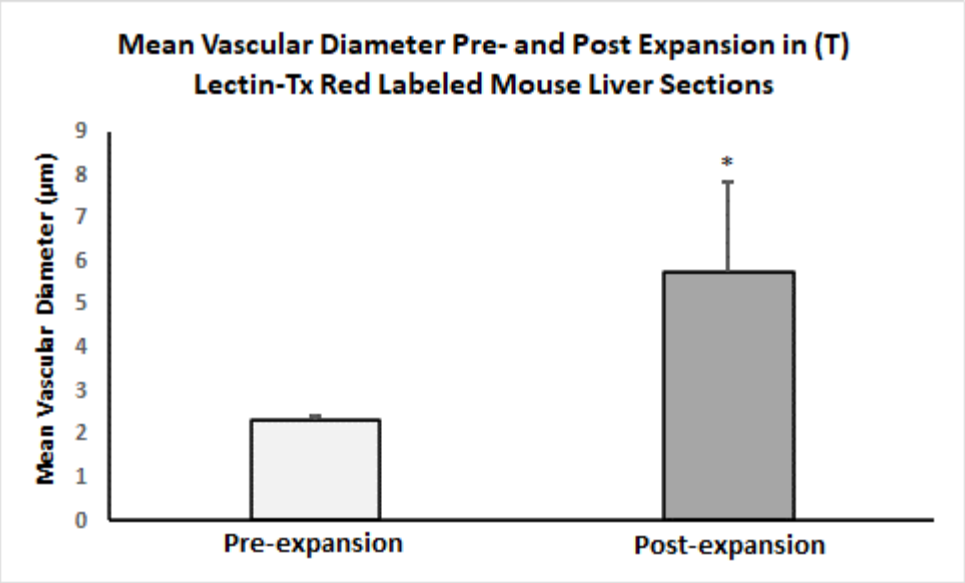

Fig 20. Comparison of mean vessel diameter across multiple samples pre-and post-expansion for (T) Lectin-Tx Red labeled liver sections. A 3.53µm increase is observed between pre-expansion (2.35µm) and post-expansion mean vessel diameter (5.87µm). p-value<0.05. The error bars represent the standard deviation.

3.6 Vascular Architecture for Lung Tissue

3.6.1 Pre-Expansion

The parameters for vasculature extracted from lung tissue before expansion are displayed in **Table 3.9**.

Table 3.9 – Mean values for vessel diameter, vessel volume, vessel area and vessel length of two (T) Lectin-Texas Red labeled coronal mouse lung sections from two or more FOV pre-expansion.

Morphological Parameters	M1	M2
Mean vessel diameter ± Std Dev (µm)	3.23 ± *0.27*	5.59 ± *0.80*
Mean vessel volume ± Std Dev (µm)^3	79.08 ± *55.51*	499.67 ± *894.64*
Mean vessel area ± Std Dev (µm)^2	97.45 ± *68.34*	366.98 ± *664.61*
Mean vessel length ± Std Dev (µm)	9.60 ± *6.86*	21.49 ± *39.41*

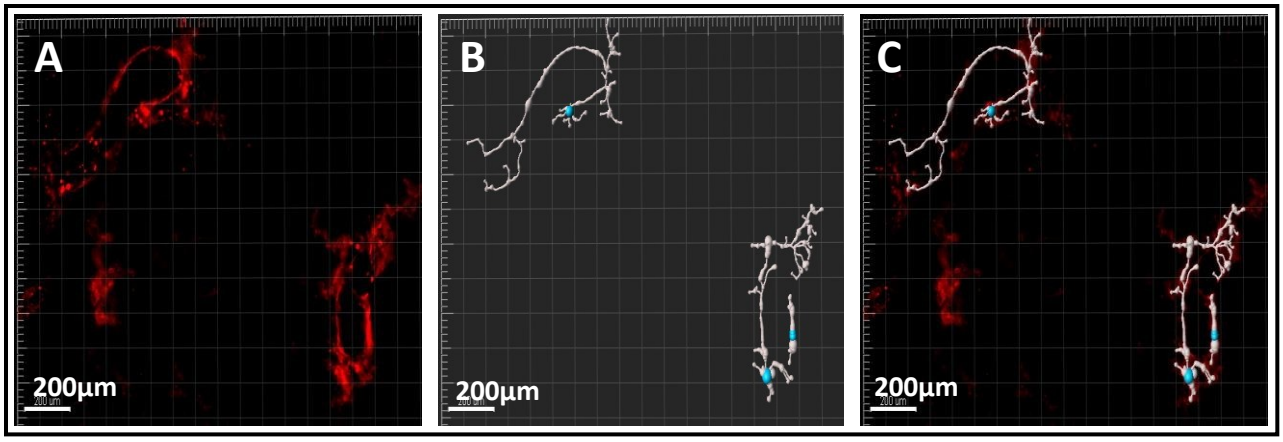

Fig 21. Results of preprocessing and segmentation of (T)Lectin-Tx Red labeled vessels in lung vasculature of pre-expansion mouse M1 : (A) Rendering of the preprocessed confocal image of a FOV of (T) Lectin-Tx Red stained vessels from mouse M1 using preprocessing tools in IMARIS® software, Threshold Cutoff = 45.9, Gaussian filter = 2.0µm and background subtraction = 173µm (B) Segmentation of vessels (grey) in (A) using the *FilamentTracer* tool from IMARIS® which also computes the morphological parameters. The blue spheres indicate the starting points for identifying vessels created by the IMARIS® algorithm. (C) Overlay of the results of preprocessed image (A) (red channel) and vessel segmentation (B) (grey) to assess quality of segmentation.

3.6.2 Post-Expansion

The parameters for vasculature extracted from lung tissue before expansion are displayed in **Table 3.10.**

Table 3.10 – Mean values for vessel diameter, vessel volume, vessel area and vessel length of two (T) Lectin – Texas Red labeled coronal mouse (M1 and M2) lung sections from two or more FOV post-expansion.

Morphological Parameters	M1	M2
Mean vessel diameter ± Std Dev (µm)	6.31 ± *1.24*	8.41 ± *3.72*
Mean vessel volume ± Std Dev (µm)^3	540.36 ± *586.66*	1702.44 ± *2607.62*
Mean vessel area ± Std Dev (µm)^2	350.60 ± *390.92*	721.90 ± *829.38*
Mean vessel length ± Std Dev (µm)	18.56 ± *20.25*	27.39 ± *31.33*

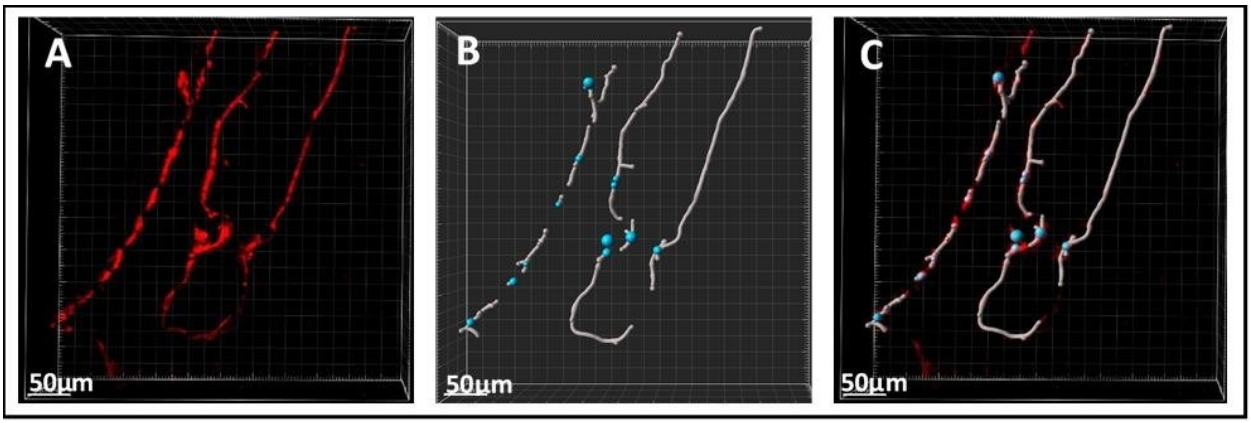

Fig 22. Results of preprocessing and segmentation of (T) Lectin-Tx Red labeled vessels in lung vasculature of post-expansion mouse M2 : (A) Rendering of the preprocessed confocal image of a FOV of (T) Lectin-Tx Red stained vessels from mouse M2 using preprocessing tools in IMARIS® software, Threshold Cutoff = 32.7, Gaussian filter = 2.0µm and background subtraction = 105µm (B) Segmentation of vessels (grey) in (A) using the *FilamentTracer* tool from IMARIS®. The blue spheres indicate starting points for identifying vessels created by the IMARIS® algorithm. (C) Overlay of the results of preprocessed image (A) (red channel) and vessel segmentation (B) (grey) to assess quality of segmentation.

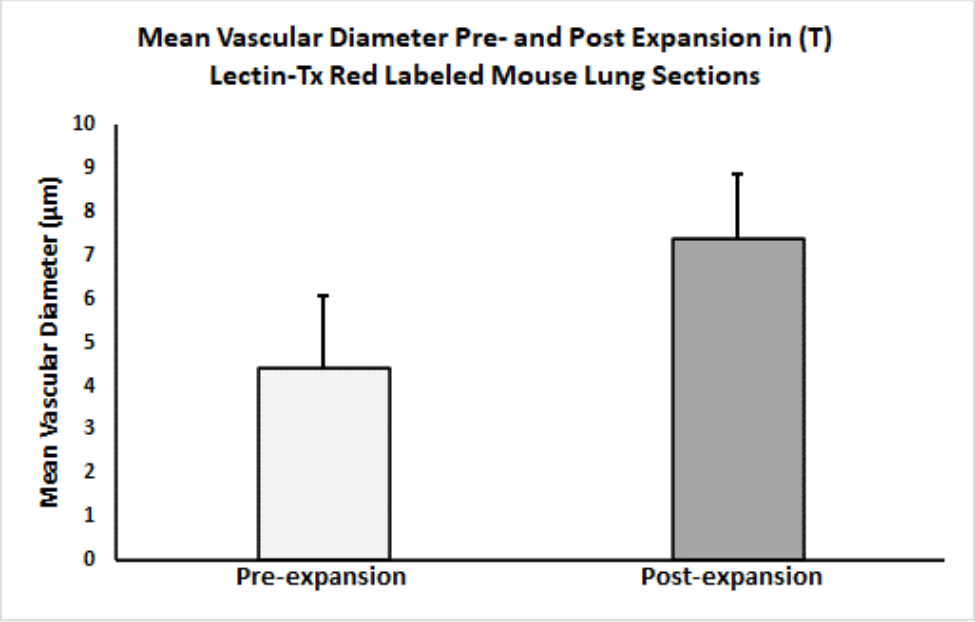

Fig 23. Comparison of mean vessel diameter across multiple samples pre-and post-expansion for (T) Lectin-Tx Red labeled lung sections. A 2.87µm increase is observed between pre-expansion (4.49µm) and post-expansion mean vessel diameter (7.36µm). p-value<0.05. The error bars represent the standard deviation.

3.7 Vascular Architecture for Leg Muscle Tissue

3.7.1 Pre-Expansion

The parameters for vasculature extracted from leg muscle sections before expansion are displayed in **Table 3.11**.

Table 3.11– Mean values for vessel diameter, vessel volume, vessel area and vessel of three (T)Lectin–Texas Red labeled coronal mouse (M1-M3) leg muscle sections from two or more FOV pre-expansion.

Morphological Parameters	M1	M2	M3	M4
Mean vessel diameter ± Std Dev (μm)	13.55 ± *4.87*	7.73 ± *1.39*	6.12 ± *1.39*	7.41 ± *1.86*
Mean vessel volume ± Std Dev (μm)³	2607.02 ± *2009.04*	1734.37 ± *2934.86*	851.02 ± *1008.60*	693.07 ± *521.60*
Mean vessel area ± Std Dev (μm)²	825.34 ± *574.53*	844.90 ± *1356.08*	538.26 ± *642.82*	385.17 ± *278.82*
Mean vessel length ± Std Dev (μm)	19.87 ± *15.02*	31.90 ± *50.22*	25.54 ± *34.08*	17.93 ± *16.49*

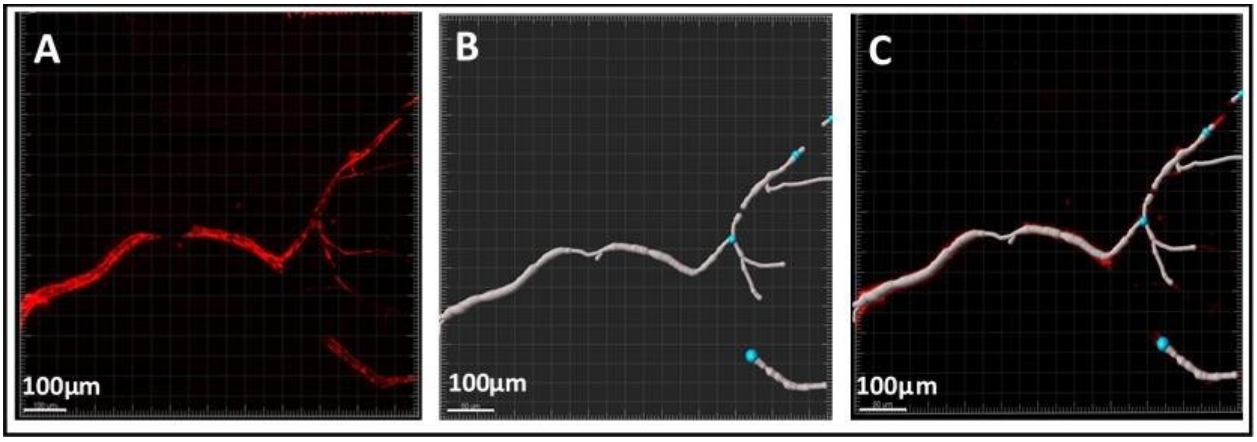

Fig 24. Results of preprocessing and segmentation of (T) Lectin-Tx Red labeled vessels in leg muscle vasculature of pre-expansion mouse M1 : (A) Rendering of the preprocessed confocal image of a FOV of (T) Lectin-Tx Red stained vessels from mouse M1 using preprocessing tools in IMARIS® software, Linear Stretch, Gaussian filter = 1.0µm, background subtraction = 106µm. (B) Segmentation of vessels (grey) in (A) using the *FilamentTracer* tool from IMARIS® which computes morphological parameters. The blue spheres indicate starting points for identifying vessels created by the IMARIS® algorithm (see section 2.5 for detail). (C) Overlay of the results of preprocessed image (A) (red channel) and vessel segmentation (B) (grey) to assess quality of segmentation.

3.7.2 Post-Expansion

The parameters for vasculature extracted from lung tissue before expansion are displayed in Table 3.12

Table 3.12 – Mean values for vessel diameter, vessel volume, vessel area and vessel length segmentation of two (T) Lectin Texas Red labeled coronal mouse (M1-M2) leg sections from two or more FOV post-expansion.

Morphological Parameters	M1	M2
Mean vessel diameter ± Std Dev (µm)	24.15 ± *6.04*	17.88 ± *6.60*
Mean vessel volume ± Std Dev (µm)^3	17424.60 ± *12045.04*	10199.30 ± *11440*
Mean vessel area ± Std Dev (µm)^2	2706.21 ± *1968*	2434.77 ± *818*
Mean vessel length ± Std Dev (µm)	31.53 ± *28.5*	51.44 ± *55.6*

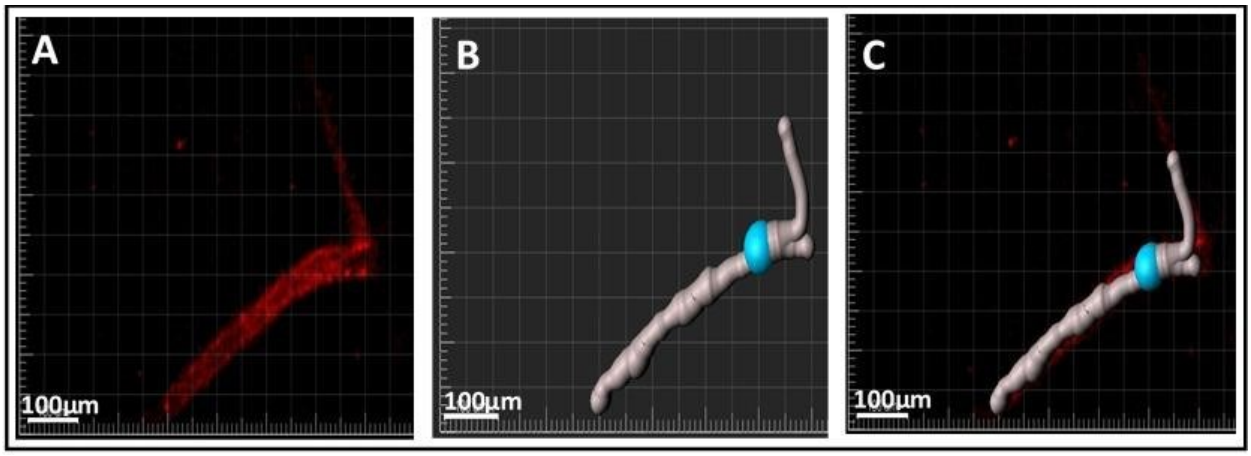

Fig 25. Results of preprocessing and segmentation of (T) Lectin-Tx Red labeled vessels in leg muscle vasculature of post-expansion mouse M1 : (A) Rendering of the preprocessed confocal image of a FOV of (T) Lectin-Tx Red labeled vessels from mouse M1 using preprocessing tools in IMARIS® software, Linear Stretch, Gaussian filter = 2.0µm, background subtraction = 87µm. (B) Segmentation of vessels (grey) in (A) using the *FilamentTracer* tool from IMARIS® which computes morphological parameters. The blue sphere indicates starting point for identifying vessels created by the IMARIS® algorithm (see section 2.5 details). (C) Overlay of the results of preprocessed image (A) (red channel) and vessel segmentation (B) (grey) to assess quality of segmentation.

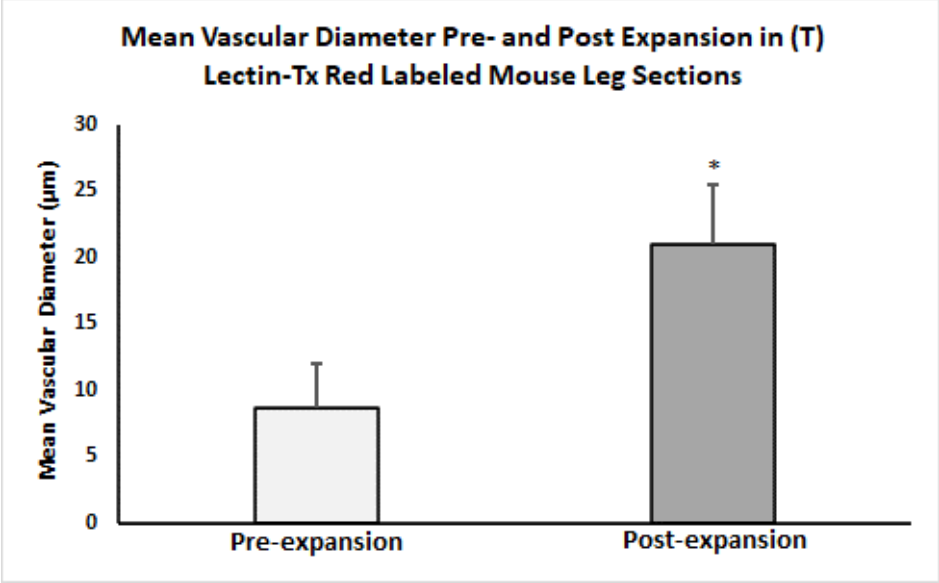

Fig 26. Comparison of mean vessel diameter across multiple samples pre-and post-expansion for (T) Lectin-Tx Red labeled leg muscle sections. A 12.32µm increase is observed between pre-expansion (8.70µm) and post-expansion mean vessel diameter (21.02µm). *p-value<0.05. The error bars represent the standard deviation.

The morphological parameters vessel area, vessel volume and vessel length computed by IMARIS® show high standard deviations. In most samples the coefficient of variation (CV = stdev/mean) was greater than or equal to one, this indicates that the distribution is not centered. The reason for this is the algorithm on which the vessels are segmented. The software does not segment whole vessels, rather a vessel is segmented into a group of smaller sections**.** The algorithm generates each segment using the SPD and EPD specified as guides (see section 2.5 for details). Since the mean values of these parameters does not represent the mean of a complete vessels but smaller sections, the resulting mean values do not yield any trend in samples pre-and post-expansion. Only the mean vessel diameter data had a CV of less than one and was therefore used for further comparison between pre-and post-expansion samples.

CHAPTER 4

4. Discussion

4.1 VascExM Protocol

The first aim of this thesis was to adapt expansion microscopy (ExM) protocols originally intended for mapping proteins in histological tissue as described in Asano et al. 2018, into a novel protocol for optical imaging of labeled vasculature in preclinical tissue samples. We termed this new protocol 'VascExM'.

During the initial stages of protocol development, immunostaining was performed in 24-well plates, to ensure minimal handling of samples, the same plate was then used as the gelation chamber. This resulted in the utilization of 200 µl of gelling solution per sample. This led to the formation of 1-1.5 mm thick gels in which samples were susceptible to folding (**Fig 27 F and G**). Another concern was that on expanding the gel in water, made it significantly swell vertically (~3 mm). This created challenges for imaging because the thickness of the gel was not accommodated by the limited working distance of the 20× lens (NA=1.0) on the Zeiss 710 microscope. Moreover, thick gels were fragile during handling after expansion, and could not be stored for re-expansion.

After multiple containers were tested for reducing the gel's thickness, it was determined that the thinnest gels could be made by expanding the samples directly on the slide. For this purpose, gelation chambers were created by gluing no. 1.5 coverslips at the ends of the slide to act as spacers and give height to the chamber (**Fig. 27 A**). The sample was then carefully placed in the gelation solution in the gap between the spacers. A no. 1 coverslip was placed on the container as a lid to prevent evaporation of the gelation solution during incubation. However, leakage of the

solution was observed from the edges, near the spacers. This was overcome by wrapping spacers with parafilm instead of gluing them down seen in **Fig 27 B**. The malleable parafilm sealed the chamber, preventing any leakage. Along with reducing unexpanded gel thickness from 1-1.5 mm to 0.5-0.7 mm (**Fig 27 C, D and E**), the amount of gelation solution required for the protocol also decreased to 80-100 µl. Thus, the time taken for polymerization in the incubator was reduced from 2-3 hours to 45-60 minutes.

On observing the expanded samples under the microscope, excessive fragmentation of the tissue was noted. To optimize the expansion, incubation time for the digestion process was decreased from overnight to 5 hours. Similarly, the incubation time for expansion of the gel in water was also reduced from 60 to 45 minutes, to help maintain the structural integrity of the expanded sample.

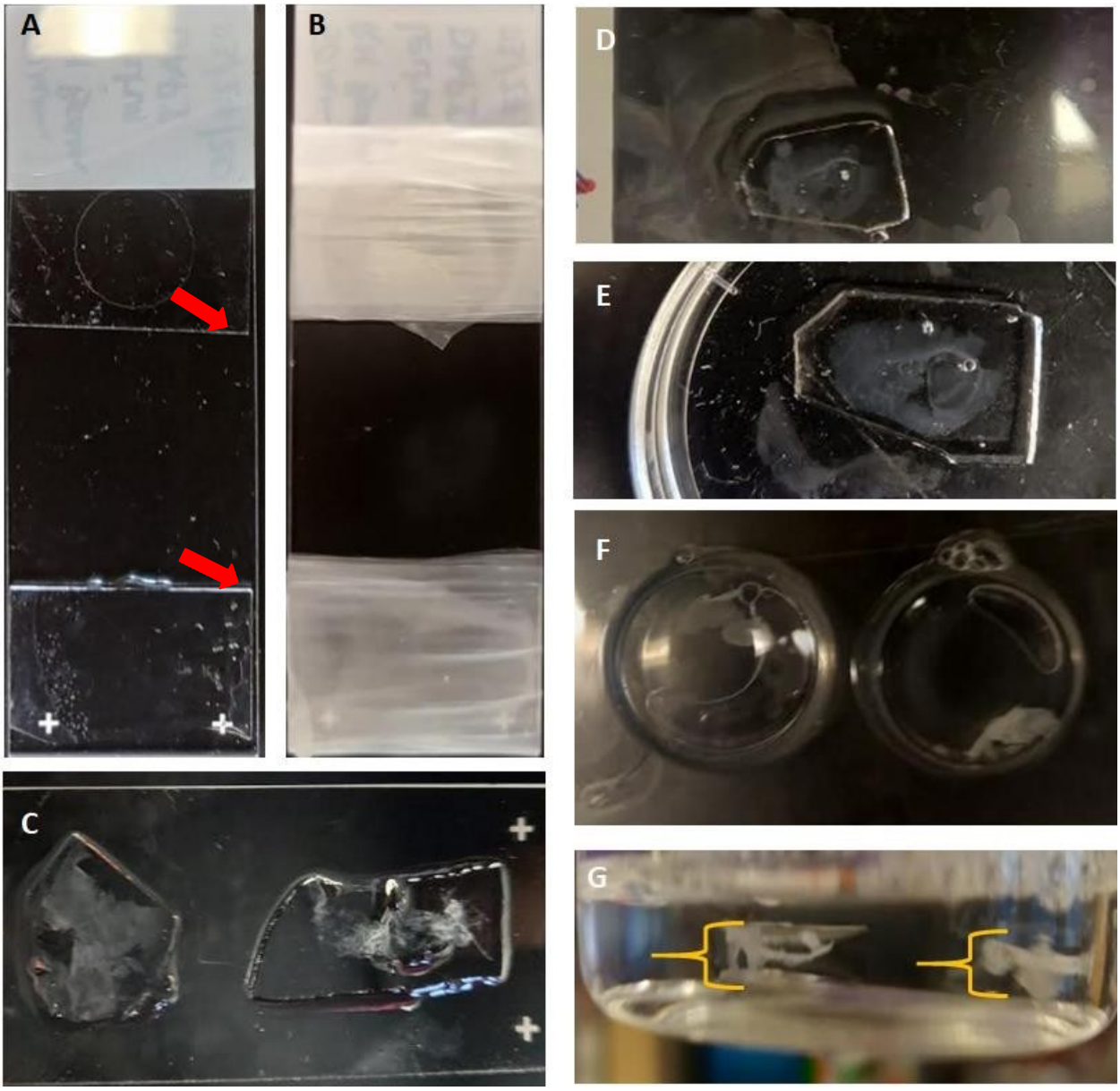

Fig 27. Pictures of gelation chambers and gels during VascExM protocol development. (A) First iteration of slide-based gelation chamber in which spacers were glued down at the corners of the slide, but leakage of gelation solution occurred at the edges as indicated by the red arrows. (B) The final chamber prototype used in the VascExM protocol - here parafilm was used to secure the spacers and a coverslip was used as a lid for the chamber. (C) Representative gels formed using the slide-based gelation chamber. (D) Pre-expansion coronal section of the mouse brain displayed on a slide. (E) Post- expansion coronal section from (D) placed in a petri dish with water for the diffusion step. (F) Representative gels formed in the wells of a 24-well plate "gelation chamber". (G) During expansion in water, folding can be seen along the height of each sample as indicated by the yellow brackets.

4.2 Vessel Segmentation Pipeline

4.2.1 IMARIS® Segmentation

The regular and hierarchical branching of vasculature in coronal sections of mouse brain, heart and leg tissue were segmented using IMARIS® software as explained in section 2.5. The quality of the vessel segmentation was assessed by visual inspection. The values of all morphological parameters generated were exported to Microsoft Excel for statistical analysis. Data for any irregular branches generated by the *FilamentTracer* tool in IMARIS® software were excluded based on the diameter thresholds set in IMARIS® before mean values were calculated (**Fig 28**).

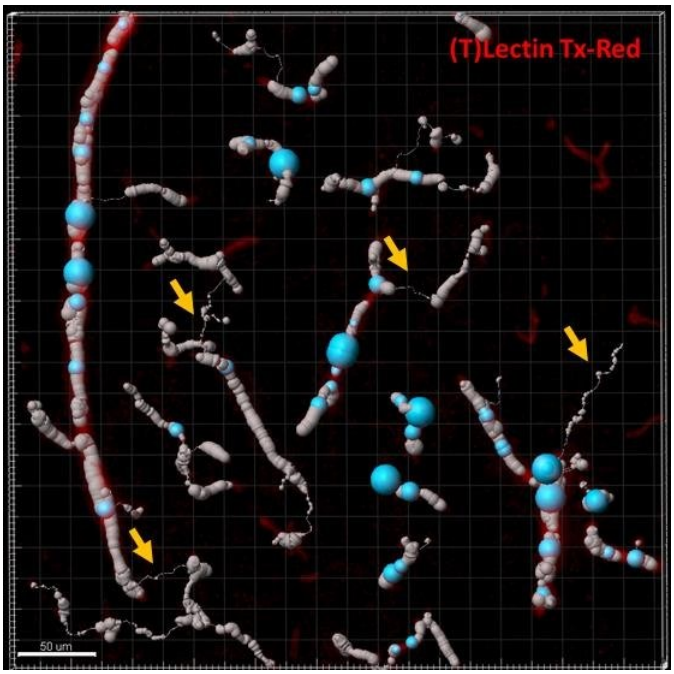

Fig 28. Segmentation of (T)-Lectin Texas Red stained vasculature in mouse brain tissue post-expansion. Arrows point to irregular branches generated by the *FilamentTracer* tool's algorithm in regions where actual vessels were not present.

4.3 Discussion of Results

The second aim of this thesis was to determine which vascular labeling method lends itself best to tissue expansion. Three kinds of vascular labels with different binding properties were tested in the brain tissue.

4.3.1 Anti-Laminin Cy3 Antibody Labeling

Visual inspection of expanded tissue images showed that vessels exhibiting intact and continuous laminin labeling appeared fragmented along their length. As described in Chapter 2, the anti-laminin antibody binds to its epitope on the basement membrane, the outer layer of the vessel, responsible for providing structural support. In both pre- and post-expansion images, the laminin binding could be observed along outer edges of the vessels. Since IMARIS® segments vessels based on their image intensity, this posed a hurdle when calculating the accurate diameter of vessels as shown in **Fig 29.**

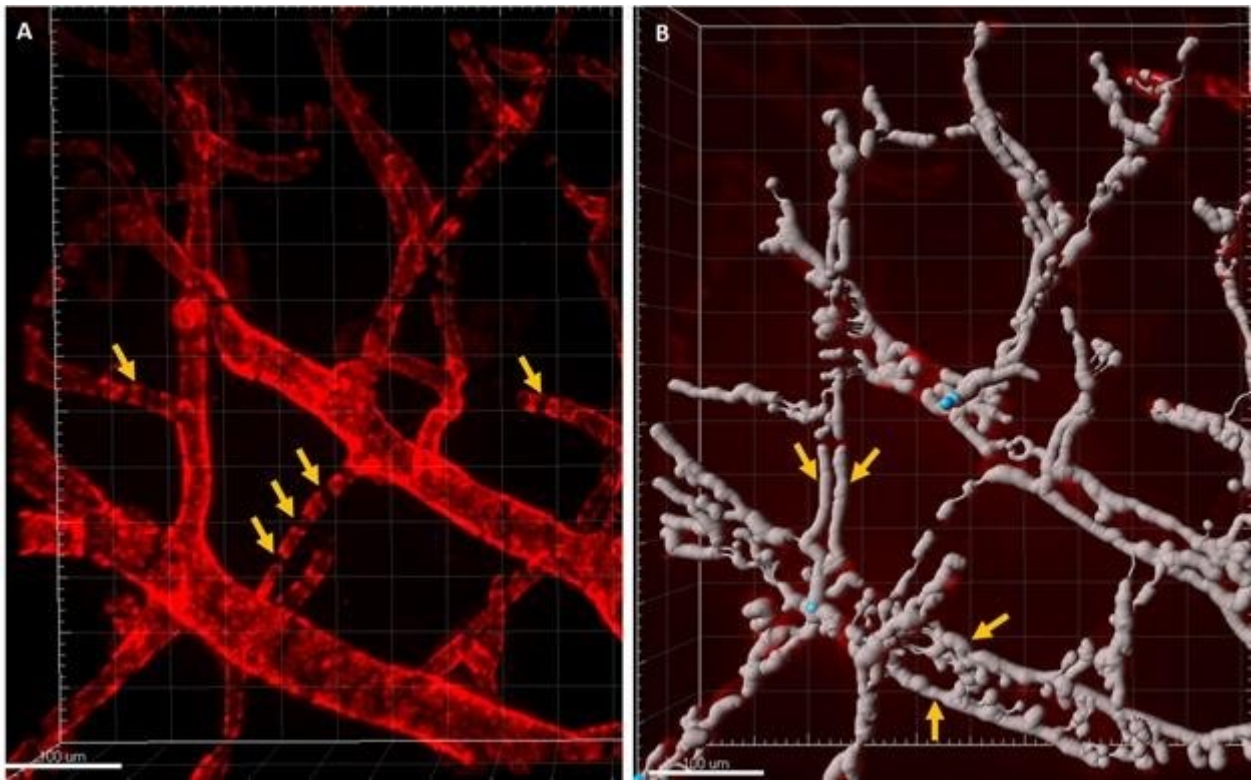

Fig 29. Issues observed for anti-Laminin Cy3 antibody staining in the mouse brain. (A) Arrows indicate fragmentation of the vessel label after expansion. (B) Segmentation of image A using IMARIS®. Segmentation is done based on local intensity, therefore only the outermost boundary of each vessel gets segmented. The true diameter of the vessels is not accurately identifiable; arrows indicate regions of improper segmentation.

4.3.2 Tomato(T)-Lectin Texas Red Labeling

The intravenously administered (T)Lectin solution binds to the luminal (i.e. inner) surface of the blood vessels. Therefore, in the 3D renderings of the tissue samples, vessels appear stained evenly across their entire width. It was observed that the continuous and unfragmented labeling was maintained post-expansion in the samples. Examples of (T)-Lectin Texas Red Labeling have been detailed in Chapter 3.

4.3.3 BriteVu and Galbumin-Rhodamine Polymer Labeling

While the two samples that were expanded showed no expansion of the administered BriteVu-Galbumin-Rhodamine polymer within the vessels, results of the analysis were inconclusive due to the limited number of tissue samples. Furthermore, perfusion efficiency in the available samples seemed poor, resulting in few labeled vessels per field prior to expansion.

Due to the fragmentation of expanded vasculature observed in samples stained with anti-laminin, and poor BriteVu polymer perfusion, tomato lectin was considered a better vascular label for VascExM for this thesis. Thus, vascular expansion was performed using tomato lectin as the contrast agent for the remaining organs.

4.3.4 Trends seen in organs

Quantitative analysis of the changes in morphological parameters post-expansion were performed as explained in section 2.6.

To compare the efficacy of expansion for (T) Lectin-Tx Red and anti-Laminin Cy3 labels, change in signal intensity was assessed in samples pre- and post-expansion. Expanded anti-Laminin labeled sections indicated an approximately 87% decrease in mean intensity of label observed in post-expansion tissue samples. Whereas (T)-Lectin only resulted in a 2% decrease in mean intensity post-expansion. Tillberg et al and Gao et al explain that the Cyanine fluorophores lose structural stability during the polymerization which makes fluorophores like Cy3 more susceptible to degradation, yielding lower label per unit pixel.

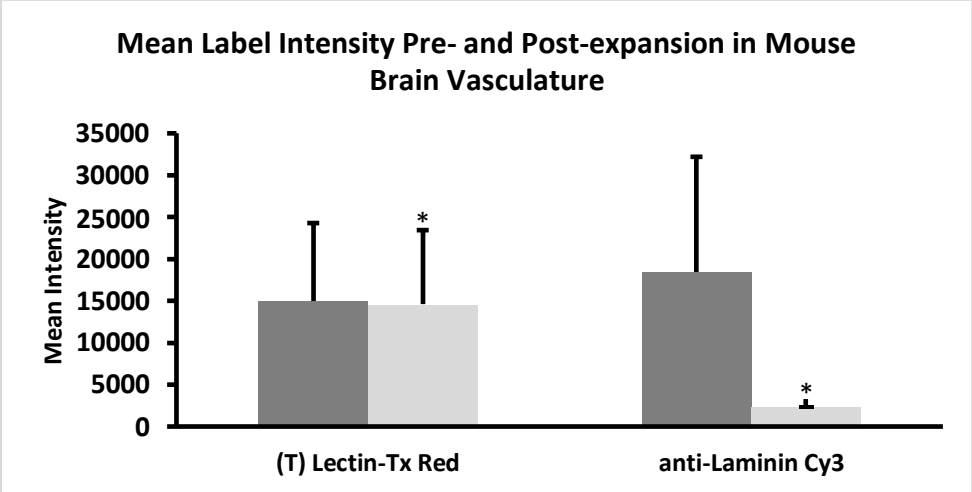

Fig 30. Comparison of mean label intensity across multiple brain tissue samples pre-and post-expansion. (T) Lectin-Tx Red labeled samples underwent a decrease of ~400 units in mean intensity after expansion. For anti-Laminin Cy3 a 16132-unit (i.e. 87%) decrease was observed post-expansion *p-value<0.05. The error bars represent the standard error of the mean.

Though a significant difference is seen in the intensity of both vascular labels, expanded brain tissue sections stained with (T) Lectin and anti-Laminin exhibited a 158% and 156% increase in the mean vessel diameter, respectively. A similar trend was observed in leg muscle, liver, and lung vasculatures. Post-expansion samples saw a 154%, 150% and 64% increase in their mean vessel diameters, respectively. However, changes in parameters in heart tissue did not exhibit an increase in mean vessel diameter. Post-expansion showed an approximately 61% decrease in size. One reason for this could be due to sampling error, without the registration of post-ExM samples on pre-ExM we faced difficulty in acquiring images from the same area once the samples had expanded.

4.4 VascExM Protocol

Based on the results of these preliminary studies the finalized VascExM protocol we developed is summarized below:

Tissue Preparation

Perfused animal is fixed in 10% buffered formalin at 4° C for 2-3 days before being transferred to 30% sucrose cryoprotectant solution (Sigma Aldrich, Saint Louis, MO) and incubated overnight at 4° C. Once the sample sinks in the sucrose solution it is embedded in the optimal cutting medium (OCT, Sakura Finetek, Torrance, CA) and flash frozen in liquid nitrogen for 15 minutes and placed in the cryotome. Sample are acclimatized to the temperature in the cryostat chamber (-22° C) for 30-60 minutes before being glued onto the chuck to and sliced into sections of required thickness (10-100 μm) and stored at 4 °C until they are ready for staining.

Immunostaining

Wash sections in a 1× PBS solution for 15 minutes and then permeabilize in 1× PBST solution (PBS containing 0.5% Tween 20) for 15 minutes on an orbital shaker at 30 rpm. Incubate the washed samples in 1× carbo-free blocking solution (Vector Labs, Burlingame, MA) for 1 hour at room temperature. After blocking, the sections are incubated overnight in 150 μl of the pre-conjugated primary anti-α-SMA-FITC (1:100 dilution) and primary anti-laminin (1:200 dilution) antibody. The incubation period is directly proportional to the thickness of the tissue sections (1 night/10 μm). Next, rinse the section 3 times in PBS solution for 10 minutes each. For the pre-conjugated antibody, the sections need to be immediately transferred onto a slide, counterstained with DAPI for 1-3 minutes, mounted in aqueous mounting medium and cover slipped. For the unconjugated antibody, the two-step labeling procedure is followed. Once the anti-laminin antibody is rinsed, the sections need to be incubated in goat anti-rabbit Cy-3 secondary antibody for 3 hours. Rinse the secondary antibody off with a 15-minute PBS wash, and then counterstain with DAPI and coverslip.

Image multiple fields of each sample using 10x and 20x Zeiss 710 NLO multiphoton microscope equipped with appropriate filter sets (please see section Image Acquisition at the end of Protocol).

Gelation

After the pre-expansion samples are imaged, prepare them for expansion. Incubate the slides in PBS for 2 hours to remove the coverslips with ease. Remove the samples from the slide and rinse in PBS for 10 minutes.

AcX treatment. Resuspend the Acryloyl-X, SE solution in anhydrous DMSO at a concentration of 10 mg/mL (aliquot and store in desiccated environment at -20^{0}C for up to 3 months). Dilute the AcX/DMSO solution in PBS at a concentration of 0.1 mg/ml. Incubate the rinsed samples in this dilution for 6 h, at RT.

While the sample is incubating in AcX, construct a gelation chamber and gelation solution. For gelation chamber, superglue two No. 1.5 coverslips on the edges of a slide, then wrap both edges evenly using parafilm.

The gelling solution needs to be freshly prepared each time by adding Stock X, 4HT solution, TEMED and APS together in this specific order at a volumetric ratio of 47:1:1:1. All solutions should be aliquoted and stored at -20^{0}C, APS and 4HT aliquots should be prepared fresh every 3-4 weeks.

Table 4.1 Gelation Solution

Reagent	Stock Solution Concentration	Stock solution Volume
Stock X	*	9.4ml
4HT	0.5% w/v	1ml
TEMED	10% w/w (as determined in container)	1ml
APS	10% w/w	1 ml

***Table 4.2 Stock X Solution**

Stock X Reagents	Stock Solution Concentration(g/100ml)	Stock Solution Volume(ml)
Sodium acrylate	35	2.25
Acrylamide	40	0.5
N, N ' - Methylenebisacrylamide	2	0.75
Sodium Chloride	29.2(5 M)	4
PBS	10×	1
Water		0.9
Total		9.4

Once the samples are done incubating in AcX solution, wash twice with PBS for 15 mins each time.

Place 80-100 µl of the gelling solution in the chamber and carefully transfer the tissue sample onto the solution using a paint brush, ensure there are no folds in the tissue section. Seal the chamber with a coverslip on the top to prevent any leakage of solution.

Once the lid is placed on the slide and air bubbles removed, keep the chamber in the dark at 4ºC for 30 minutes. After this initial incubation, transfer the chamber to a 37º C incubator for polymerization 1-2 hours depending on the thickness of the tissue section. Ensure that the chamber was not tilted or shaken during the gelation process.

Digestion

While polymerization occurs prepare the digestion buffer.

Table 4.3 Digestion Buffer

Digestion Buffer Reagents	**Final concentration(/100ml)**
Triton X-100	0.50g
EDTA, disodium (0.5M, pH 8)	0.2ml
Tris.Cl (1M, pH 8)	5ml
NaCl	4.67g
Proteinase K	1:100 dilution**
Water	Add up to total 100ml

** The digestion buffer is aliquoted and stored at -20^{0}C without the Proteinase K. Proteinase K is added immediately before the digestion step after buffer is thawed.

After 1- 2 h the chamber is removed from the incubator. Separate the lid gently from the top by using a blade. Using a fine paint brush, transfer the gel into a container of digestion buffer to incubate for 5h at room temperature in the dark.

Expansion and Storage

In case the samples do not need to be imaged immediately after gelation, the gel embedded samples can be stored in PBS in the dark at 4ºC and expanded as needed.

Trim the digested gel to a reasonable size for ease in handling. Prior to imaging samples, immerse the gel in water for 10-15 minutes. Repeat this step three times with fresh water each time for a total of 30-45 minutes. At this juncture the sample should be optically clear, completely expanded, and ready for imaging.

Imaging Acquisition

Pre- and post-expansion images of the tissues are acquired on a Zeiss LSM 710 NLO using a W Plan-APOCHROMAT 20×/1.0 water immersion objective. Isolate the required FOV with distinctly labeled vasculature using the 10× air objective. Once the FOV is selected, switch to the 20× objective and refocus the sample, add a drop or two of water to form a water column between the sample and the objective. On the imaging software (Zen v2.3), set the lasers in the specific

range according to the fluorophores being imaged (see Table 2.2 for detail). Adjust the value of laser power, pinhole width and gain so that least amount of background in observed while imaging the vasculature. To obtain a 3D image, set the range along the z-axis to be imaged and run the z-stack protocol in the software. A collection of 2D images (of the XY plane) will be taken along the z-axis at regular intervals which can be stitched to obtain a 3D structure of the labeled vasculature.

CHAPTER 5

5. Conclusion and Future Prospects

5.1 Conclusion

In conclusion I would like to recapitulate the initial aims and final findings of the thesis:

I. The first aim of this thesis was to develop a tissue processing protocol for high-resolution optical imaging of the vasculature in preclinical models.

   VascExM is a new protocol to obtain high resolution 3D optical images of the vasculature in the mouse model using chemical reagents and diffraction-limited microscope hardware already common in biology labs. The protocol was successful in expanding vasculature in the brain, leg and liver to a magnification of ~2.5× and lung vasculature to ~1.64× (all calculation were performed using mean values) A constraint of the developed technique was the long incubation time required for the protocol. The entire process could take seven to ten days for a sample depending on its thickness.

II. The second aim was to determine the efficacy of expansion protocol across various vascular labels.

   To optimize VascExM we tested three different vascular labeling methods: Based on the experiments conducted, it was determined that tomato-lectin exhibited the most intact and continuous vascular label pre- and post-expansion. The experiments also demonstrated that Texas-Red did not undergo any significant loss in signal intensity post-expansion making it an ideal fluorophore for imaging expanded samples. Due to limited availability of well-perfused BriteVu and Galbumin-Rhodamine polymer tissues this observation needs to be

explored further using a larger number of polymer perfused samples.

III. A third aim initially discussed for this thesis was to locate landmark vessels pre- and post-expansion for registration of expanded sample images with pre-expansion images. Due to the time constraints arising from the Covid-19 induced closure of the lab, this aim was not completed. Instead, unpaired statistical analysis was performed on the pre-and post-expansion morphological data for each tissue sample. To ensure accuracy, pre-and post-expansion images were taken from the same regions in each sample.

IV. The thesis committee identified questions that should be answered in the future to ensure widespread applicability of this protocol. These include the following, was the tissue expansion isotropic in nature, how can this be validated? Was the expansion affected by the type or thickness of tissue, how can this be determined? Lastly, on what basis were the different vascular labels selected for testing? Were multiple fixatives also tested, if so, what was their effect on the tissue expansion? To validate the isotropic nature of the expansion and determine how the thickness of the tissue affects the expansion process a non-rigid registration of the pre- and post-expansion images needs to be performed with respect to each other. Through rigid transformations of rotation, scaling and translation, the extent of distortion between the two images can be calculated. Analysis of the distortion among sections of varying thicknesses can help ascertain the degree to which the expansion process depends on the thickness of tissue samples. Once aligned, for further confirmation, a vessel count can be done to determine if vascular structures have been lost due to expansion. Furthermore, the vascular labels selected were done strategically after a detailed literature review. As per Chen et al, 2015 most fluorescent proteins and dyes are compatible, therefore the selection was done based on the binding

action of the label to its specific epitope in the vasculature. Anti-Laminin Cy3 utilizes antibody binding action to attach only to the laminin in the basement membrane, whereas the injectable nature of Tomato Lectin Tx-red allows the label to fill the vessel and attach to the glycoproteins in the luminal surface, lastly, the Brite Vu and Galbumin Rhodamine polymer complex, is an MRI and CT visible contrast agent being used for other multimodal visualization projects in the Pathak Lab and was selected to determine the possibility of merging images from VascExM with those projects. While various vascular labels were tested, the rest of the staining protocol was unchanged, and no tests were performed to compare the impact of different fixatives on the expansion of the tissue sample.

5.2 Future research opportunities

This thesis lays the groundwork for a wide range of applications that can benefit from a 3D high- resolution vascular imaging technique like VascExM. Some examples of future research opportunities are given below.

I. VascExM is a new protocol for obtaining high resolution optical images using sample expansion to circumvent the diffraction limit. This optical imaging technique can be used to combine optical vascular data with that from μCT and μMRI to enable multimodality visualization of fixed tissue sections. A vessel segmentation pipeline can be developed to co-register vasculature images from expanded samples on with μCT and μMRI. High-resolution multimodality 3D images can then be used for visualizing more comprehensive

details of the vasculature.

II. While VascExM has been used to expand the vasculature in normal mouse organs, we have started the process for optimizing this high-resolution 3D imaging technique for the vasculature in tumor xenografts. 3D nanoscale visualization of tumor vasculature via VascExM can be co-registered with μCT and μMRI data for multimodal visualization of the tumor microenvironment.

III. Zhao et al in 2017 developed a form of ExM optimized for clinical pathology workflows called ExPath. These high-resolution images of neoplastic lesions generated after expansion were used to develop a model using machine learning to optically train and classify breast tumors into early or late stage tumors. Similarly, VascExM of preclinical tumor models could be implemented to classify the changes in vasculature between early and late stage tumors.

REFERENCES

[1] Smolyaninov II. Optical microscopy beyond the diffraction limit. HFSP J. 2008;2(3):129-131. doi:10.2976/1.2912559

[2] Blom, H, Brismar, H (Royal Institute of Technology, Stockholm, Sweden). STED microscopy: Increased resolution for medical research? (Review). J Intern Med 2014; 276: 560– 578.

[3] Reena Sharma, Manjot Singh, Rajesh Sharma, Recent advances in STED and RESOLFT super-resolution imaging techniques, Spectrochimica Acta Part A: Molecular and Biomolecular Spectroscopy, https://doi.org/10.1016/j.saa.2019.117715.

[4] Rust MJ, Bates M, Zhuang X. Sub-diffraction-limit imaging by stochastic optical reconstruction microscopy (STORM) Nat. Methods. 2006; 3:793–795.

[5] Wassie AT*, Zhao Y*, Boyden ES (2018) Expansion microscopy: principles and uses in biological research, Nature Methods 16(1):33-41. (*, equal contributors)

[6] Chen, F.*, Tillberg, P.W.*, Boyden, E.S. (2015) Expansion Microscopy, Science 347(6221):543-548. (*, equal contribution)

[7] Asano SM*, Gao R*, Wassie AT*, Tillberg PW, Chen F, Boyden ES (2018) Expansion Microscopy: Protocols for Imaging Proteins and RNA in Cells and Tissues, Current Protocols in Cell Biology 80(1): e56. (*, co-first authors)

[8] Chang, J.-B., Chen, F., Yoon, Y.-G., Jung, E. E., Babcock H., Kang J.-S., Asano S., Suk H.-J., Pak N., Tillberg P.W., Wassie A., Cai D., Boyden E.S. (2017) Iterative expansion microscopy, Nature Methods 14:593-599.

[9] Emmanouil D. Karagiannis*, Jeong Seuk Kang*, Tay Won Shin, Amauche Emenari, Shoh Asano, Leanne Lin, Emma K. Costa, IMAXT Grand Challenge Consortium, Adam H. Marblestone, Narayanan Kasthuri, Edward S. Boyden (2019) Expansion Microscopy of Lipid Membranes, bioRxiv 829903. (*, equal contribution)

[10] Zhao Y*, Bucur O*, Irshad H, Chen F, Weins A, Stancu AL, Oh EY, DiStasio M, Torous V, Glass B, Stillman IE, Schnitt SJ, Beck AH**, Boyden ES** (2017) Nanoscale imaging of clinical specimens using pathology-optimized expansion microscopy, Nature Biotechnology 35(8):757-764. (*, co-first authors; **, co-corresponding authors)

[11] Caldemeyer KS, Buckwalter KA. The basic principles of computed tomography and magnetic resonance imaging. J Am Acad Dermatol. 1999;41(5 Pt 1):768-771. doi:10.1016/s0190-9622(99)70015-0

[12] Kumamaru KK, Hoppel BE, Mather RT, Rybicki FJ. CT angiography: current technology and clinical use. Radiol Clin North Am. 2010;48(2):213–vii. doi: 10.1016/j.rcl.2010.02.006

[13] Halpern EJ. Clinical applications of cardiac CT angiography. Insights Imaging. 2010;1(4):205–222. doi:10.1007/s13244-010-0038-3

[14] R T Higashida, V V Halbach, F Y Tsai, C F Dowd, and G B HieshimaInterventional neurovascular techniques for cerebral revascularization in the treatment of stroke. American Journal of Roentgenology 1994 163:4, 793-800

[15] Baliyan V, Shaqdan K, Hedgire S, Ghoshhajra B. Vascular computed tomography angiography technique and indications. Cardiovasc Diagn Ther. 2019;9(Suppl 1): S14-S27. doi:10.21037/cdt.2019.07.0

[16] Zagorchev L, Oses P, Zhuang ZW, et al. Micro computed tomography for vascular exploration. J Angiogenes Res. 2010; 2:7. Published 2010 Mar 5. doi:10.1186/2040-2384- 2-7

[17] Deng Y, Rowe KJ, Chaudhary KR, Yang A, Mei SHJ, Stewart DJ. Optimizing imaging of the rat pulmonary microvasculature by micro-computed tomography. Pulm Circ. 2019;9(4):2045894019883613. Published 2019 Oct 31. doi:10.1177/2045894019883613

[18] Quantitative Ex-Vivo Micro-Computed Tomographic Imaging of Blood Vessels and Necrotic Regions within Tumors Charlene M. Downey, Arvind K. Singla, Michelle L. Villemaire, Helen R. Buie, Steven K. Boyd, Frank R. Jirik

[19] Downey CM, Singla AK, Villemaire ML, Buie HR, Boyd SK, Jirik FR. Quantitative ex-vivo micro-computed tomographic imaging of blood vessels and necrotic regions within tumors. PLoS One. 2012;7(7): e41685. doi: 10.1371/journal.pone.0041685

[20] Cebulla J, Kim E, Rhie K, Zhang J, Pathak AP. Multiscale and multi-modality visualization of angiogenesis in a human breast cancer model. Angiogenesis. 2014;17(3):695–709. doi:10.1007/s10456-014-9429-2

[21] Dorr A., Sled J.G., Kabani N. Three-dimensional cerebral vasculature of the CBA mouse brain: A magnetic resonance imaging and micro computed tomography study. Neuroimage. 2007; 35:1409–1423. doi: 10.1016/j.neuroimage.2006.12.040

[22] Zagorchev L, Oses P, Zhuang ZW, et al. Micro computed tomography for vascular exploration. J Angiogenes Res. 2010; 2:7. Published 2010 Mar 5. doi:10.1186/2040-2384- 2-7 \

[23] Kampschulte M, Langheinirch AC, Sender J, et al. Nano-Computed Tomography: Technique and Applications. Rofo. 2016;188(2):146-154. doi:10.1055/s-0041-106541

[24] Duvall CL, Taylor WR, Weiss D et al. Quantitative microcomputed tomography analysis of collateral vessel development after ischemic injury. Am J Physiol Heart Circ Physiol 2004; 287: H302-H310

[25] https://www.nibib.nih.gov/science-education/science-topics/magnetic-resonance-imaging-mri

[26] The AAPM/RSNA physics tutorial for residents. An introduction to MR angiography. Radiographics. 1995 Mar; 15(2):453-65. Saloner D. PMID: 7761648.

[27] Brubaker LM, Bullitt E, Yin C, Van Dyke T, Lin W. Magnetic resonance angiography visualization of abnormal tumor vasculature in genetically engineered mice. Cancer Res. 2005;65(18):8218–8223. doi: 10.1158/0008-5472.CAN-04-4355

[28] Grochowski, Cezary & Staśkiewicz, Grzegorz. (2017). Ultra-high field TOF-MRA: A method to visualize small cerebral vessels. 7 T TOF-MRA sequence parameters on different MRI scanners – Literature review. Neurologia i Neurochirurgia Polska. 51.10.1016/j.pjnns.2017.06.011.

[29] Alexandre Ferreira, H. and Ramalho, J.N. (2013). Basic Principles of Phase Contrast Magnetic Resonance Angiography (PC MRA) and MRV. In Vascular Imaging of the Central Nervous System (eds J.N. Ramalho and M. Castillo). doi:10.1002/9781118434550.ch8

[30] de Kemp RA, Epstein FH, Catana C, Tsui BM, Ritman EL. Small-animal molecular imaging methods. J Nucl Med. 2010;51 Suppl 1(0 1):18S-32S. doi:10.2967/jnumed.109.068148

[31] Ho V.B., Corse W.R., Maki J.H. (2005) Contrast-Enhanced MR Angiography: Theory and Technical Optimization. In: Schneider G., Prince M.R., Meaney J.F.M., Ho V.B. (eds) Magnetic Resonance Angiography. Springer, Milano

[32] T. Boujan, U. Neuberger, J. Pfaff, S. Nagel, C. Herweh, M. Bendszus, M.A. Möhlenbruch Value of Contrast-Enhanced MRA versus Time-of-Flight MRA in Acute Ischemic Stroke MRI American Journal of Neuroradiology Aug 2018, DOI: 10.3174/ajnr.A5771

[33] Kim E, Stamatelos S, Cebulla J, Bhujwalla ZM, Popel AS, Pathak AP. Multiscale imaging and computational modeling of blood flow in the tumor vasculature. Ann Biomed Eng. 2012;40(11):2425–2441. doi:10.1007/s10439-012-0585-5

[34] Halefoglu AM, Yousem DM. Susceptibility weighted imaging: Clinical applications and \ future directions. World J Radiol. 2018;10(4):30-45. doi:10.4329/wjr. v10.i4.30

[35] Verma SK, Kan EM, Lu J, et al. Multi-echo susceptibility-weighted imaging and histology of open-field blast-induced traumatic brain injury in a rat model. NMR Biomed. 2015; 28(9):1069-1077. doi:10.1002/nbm.3351

[36] Vaas M. Deistung, A. Reichenbach, J.R. et al. Vascular and Tissue Changes of Magnetic Susceptibility in the Mouse Brain After Transient Cerebral Ischemia. Transl. Stroke Res. 9,426-435 (2018). https://doi.org/10.1007/s12975-017-0591-x

[37] https://www.youtube.com/watch?v=yrTy03O0gWw

[38] Simon R. Cherry, Sanjiv S. Gambhir, Use of Positron Emission Tomography in Animal Research, ILAR Journal, Volume 42, Issue 3, 2001, Pages 219- 232, https: //doi.org / 10 .1093/ilar.42.3.219

[39] Schmidt KC, Smith CB. Resolution, sensitivity and precision with autoradiography and small animal positron emission tomography: implications for functional brain imaging imaging animal research. Nucl MedBiol.2005;32(7):719-725. doi: 10.1016/j.nucmedbio.2005.04.020

[40] Mirus M, Tokalov SV, Abramyuk A, et al. Noninvasive assessment and quantification of tumor vascularization using [18F] FDG-PET/CT and CE-CT in a tumor model with modifiable angiogenesis-an animal experimental prospective cohort study. EJNMMI Res. 2019;9(1):55. Published 2019 Jun 21. doi:10.1186/s13550-019-0502-0

[41] https://www.nibib.nih.gov/science-education/science-topics/nuclear-medicine

[42] Golestani R, Wu C, Tio RA, et al. Small-animal SPECT and SPECT/CT: application in cardiovascular research. Eur J Nucl Med Mol Imaging. 2010;37(9):1766–1777. doi:10.1007/s00259-009-1321-8

[43] Dynamic changes in three-dimensional architecture and vascular volume of transmural coronary microvasculature between diastolic- and systolic-arrested rat hearts.Toyota E, Fujimoto K, Ogasawara Y, Kajita T, Shigeto F, Matsumoto T, Goto M, Kajiya F Schmidt KC[1], Smith CB

[44] Benjamin L. Franc, Paul D. Acton, Carina Mari and Bruce H. Hasegawa Small-Animal SPECT and SPECT/CT: Important Tools for Preclinical Investigation. doi: 10.2967/jnumed.108.055442J Nucl Med October 2008 vol. 49 no. 10 1651-1663

[45] Momcilovic, M., Bailey, S. T., Lee, J. T., Zamilpa, C., Jones, A., Abdelhady, G., Mansfield, J., Francis, K. P., Shackelford, D. B. Utilizing 18F-FDG PET/CT Imaging and Quantitative Histology to Measure Dynamic Changes in the Glucose Metabolism in Mouse

Models of Lung Cancer. J. Vis. Exp. (137), e57167, doi:10.3791/57167 (2018).\

[46] Ramasamy SK. Structure and Functions of Blood Vessels and Vascular Niches in Bone. Stem Cells Int. 2017; 2017:5046953. doi:10.1155/2017/5046953.

[47] Tucker WD, Arora Y, Mahajan K. Anatomy, Blood Vessels. [Updated 2020 Jun 4]. In: StatPearls [Internet]. Treasure Island (FL): StatPearls Publishing; 2020 Jan-. Available from: https://www.ncbi.nlm.nih.gov/books/NBK470401/

[48] Robertson RT, Levine ST, Haynes SM, et al. Use of labeled tomato lectin for imaging vasculature structures. Histochem Cell Biol. 2015;143(2):225-234. doi:10.1007/s00418-014-1301-3

[49] https://www.scarletimaging.com/for-research/

[50] https://www.sigmaaldrich.com/catalog/product/sigma/83689?lang=en&region=US

[51] Kalluri R. Basement membranes: structure, assembly, and role in tumour angiogenesis. Nat Rev Cancer. 2003;3(6):422-433. doi:10.1038/nrc1094

[52] Hallmann R, Horn N, Selg M, Wendler O, Pausch F, Sorokin LM. Expression and function of laminins in the embryonic and mature vasculature.
Physiol Rev. 2005;85(3):979-1000. doi:10.1152/physrev.00014.200

[53] "Datasheet: Monoclonal Anti-Actin, a-Smooth Muscle-FITC clone 1A4" [edited by]

[54] Robert E. Lenga. (1988). The Sigma-Aldrich library of chemical safety data.
[Milwaukee, Wis., USA]: Sigma-Aldrich Corp.

[55] Thermo Fisher Scientific Inc "Datasheet: DAPI Nucleic Acid Stain"

[56] Der Perng M, Su M, Wen SF, Li R, Gibbon T, Prescott AR, Brenner M, Quinlan RA. The Alexander disease-causing glial fibrillary acidic protein mutant, R416W, accumulates into Rosenthal fibers by a pathway that involves filament aggregation and the association of alpha B-crystallin and HSP27.
Am J Hum Genet. 2006 Aug;79(2):197-213. Epub 2006 Jun 12.

[57] Kenneth R. Spring, Michael W. Davidson, Introduction to Fluorescence Microscopy from https://www.microscopyu.com/techniques/fluorescence/introduction-to- fluorescence-microscopy

[58] Piatkevich KD, Malashkevich VN, Morozova KS, Nemkovich NA, Almo SC, Verkhusha VV. Extended Stokes shift in fluorescent proteins: chromophore-protein interactions in a near-infrared TagRFP675 variant. Sci Rep. 2013;3:1847. doi:10.1038/srep01847

[59] H. H. Jaffe and Albert L. Miller "The fates of electronic excitation energy" J. Chem. Educ., 1966, 43 (9), p 469 DOI:10.1021/ed043p469

[60] Microscopy Techniques and Culture Surfaces: Find the Perfect Match from https://ibidi.com/content/216-confocal-microscopy

[61] Benninger RK, Piston DW. Two-photon excitation microscopy for the study of living cells and tissues. Cell Biol. 2013; Chapter 4:Unit-4.11.24. doi:10.1002/0471143030.cb0411s59

[62] Fluorophore selection from https://www.thermofisher.com/us/en/home/life-science/cell-analysis/fluorophores.html

NAUSHEEN TICKOO

4 Cove ln
Redwood City, CA 94065

ntickoo1@jhu.edu
410-917-9819

PERSONAL STATEMENT

Resolute and motivated graduate student completing a master's degree in Biomedical Engineering from Johns Hopkins University with in-depth knowledge of molecular biology, looking for a Research Associate position to utilize and further advance my skill set. Career goals include research and development of new and innovative products, designed to serve the unmet needs of patients.

EDUCATION

Johns Hopkins University, Baltimore, MD
Master of Science and Engineering in Biomedical Engineering: Expected May 2020 — GPA: 3.6

Delhi Technological University, New Delhi, INDIA
Bachelor of Technology in Biotechnology: May 2018 — GPA: 4.0

PROFESSIONAL and RESEARCH EXPERIENCE

Johns Hopkins University, Baltimore, MD – *Graduate Research Assistant* — ***January 2019 – Present***

- Developing a protocol to research the effects of Expansion Microscopy on the mouse brain to make scientifically significant improvements in imaging of mouse brain vasculature
- Standardized and optimized the immunofluorescence protocol to study the vasculature of mouse brain sections (50-200 microns)

Boston Scientific, Los Gatos, CA –*Manufacturing Operations Intern* — ***June 2019 – August 2019***

- Analyzed production data to create and implement robust manufacturing metrics and dashboards
- Developed a system to track and trend usage of fixture equipment
- Member of cross-functional teams to troubleshoot and eliminate process and system issues to reduce manufacturing downtime
- Designed and performed experiment to find the cause and extent of delamination in tissue during handling

Johns Hopkins University, Baltimore, MD – *Research Project Member* — ***August 2018 – May 2019***

- Developed a study aimed to establish a more quantitative diagnosis by identifying measurable biological markers of sleep disruption in the TMJD population
- Developed statistical models in MATLAB to determine the correlation between physiological and subjective data (questionnaires) to find the best model for prediction with as low as 12.6% mean squared error

Jawaherlal Nehru University, New Delhi, India - *UG Research Assistant* — ***August 2017 - January 2018***

- Used IHC to determine the impact of hippocampal dependent training on neurogenesis in the Sub Ventricular Zone (SVZ) region of the adult rat brain
- Florescence Imaging was used to track the neurons using BrdU labeling - administered before training - to confirm the presence of newly generated neurons in the SVZ region

National Brain Research Centre, Manesar, India *- Research Intern* — ***May 2017 – August 2017***

- Standardized and optimized TL1A and TRAIL protein expression in mouse brain by immunoblotting and IHC, to compare the contrast of expression in a healthy brain and one affected by Alzheimer's
- Conducted in-depth data analysis and literature surveys of various databases (PubMed, ENSEMBL) to understand the role of death receptors in apoptosis signaling during Alzheimer's

EXTRACURRICULAR AND LEADERSHIP EXPERIENCE

Student Career Ambassador: Johns Hopkins University, Baltimore, MD — ***October 2018 – May 2019***

- Developed a streamline system for administrating and cataloging of Career Center Grant Applications worth $30000
- Advised and edited resumes and cover letters for undergraduate students
- Communicated with recruiters to develop relation between companies and the Career Center

President: Pratibimb, the Dramatic Society of DTU, New Delhi, India — ***January 2015- January 2018***

- Acted, wrote and led 30+ students in annual productions for statewide theatre competitions

Logistics Head: Karyon, the Biotechnology Fest of DTU, New Delhi, India — ***January 2017- January 2018***

- Founded and organized Ignite'18 – The Scientific Lecture Series
- Managed logistical arrangements for The Annual Biotechnology festival which with an estimated 500+ attendance

SPECIALIZED SKILLS

Software: R, MATLAB, MINITAB, C++, Data Structure and Database Management System, MICROSOFT Office
Laboratory: Growth and Maintenance of Cell Lines, Gel-Electrophoresis (Agarose, SDS PAGE), Immunoblotting, Immunohistochemistry (Fluorescence, Chromogenic), Protein Quantification, PCR, Gel Extraction, Restriction Digestion, ELISA, LUMINEX